

# Colours, Star formation Rates, and Environments of Star forming and Quiescent Galaxies at the Cosmic Noon

Robert Feldmann<sup>1,2\*</sup>, Eliot Quataert<sup>2</sup>, Philip F. Hopkins<sup>3</sup>,  
Claude-André Faucher-Giguère<sup>4</sup>, and Dušan Kereš<sup>5</sup>

<sup>1</sup>*Institute for Computational Science, University of Zurich, Zurich CH-8057, Switzerland*

<sup>2</sup>*Department of Astronomy & Theoretical Astrophysics Center, University of California, Berkeley, CA 94720-3411, USA*

<sup>3</sup>*TAPIR 350-17, California Institute of Technology, Pasadena, CA 91125, USA*

<sup>4</sup>*Department of Physics and Astronomy and CIERA, Northwestern University, Evanston, IL 60208, USA*

<sup>5</sup>*Center for Astrophysics and Space Sciences, University of California, San Diego, CA 92093, USA*

5 March 2024

## ABSTRACT

We analyse the star formation rates (SFRs), colours, and dust extinctions of galaxies in massive ( $10^{12.5} - 10^{13.5} M_{\odot}$ ) haloes at  $z \sim 2$  in high-resolution, cosmological zoom-in simulations as part of the *Feedback in Realistic Environments* (FIRE) project. The simulations do not model feedback from active galactic nuclei (AGN) but reproduce well the observed relations between stellar and halo mass and between stellar mass and SFR. About half (a third) of the simulated massive galaxies (massive central galaxies) at  $z \sim 2$  have broad-band colours classifying them as ‘quiescent’, and the fraction of quiescent centrals is steeply decreasing towards higher redshift, in agreement with observations. The progenitors of  $z \sim 2$  quiescent central galaxies are, on average, more massive, have lower specific SFRs, and reside in more massive haloes than the progenitors of similarly massive star forming centrals. The simulations further predict a morphological mix of galaxies that includes disk-dominated, irregular, and early-type galaxies. However, our simulations do not reproduce the reddest of the quiescent galaxies observed at  $z \sim 2$ . We also do not find evidence for a colour bimodality, but are limited by our modest sample size. In our simulations, the star formation activity of central galaxies of moderate mass ( $M_{\text{star}} \sim 10^{10} - 10^{11} M_{\odot}$ ) is affected by a combination of two distinct physical processes. Outflows powered by stellar feedback result in a short-lived ( $< 100$  Myr), but almost complete, suppression of star formation activity after which many galaxies quickly recover and continue to form stars at normal rates. In addition, galaxies residing in slowly growing haloes tend to experience a moderate reduction of their SFRs (‘cosmological starvation’). The relative importance of these processes and AGN feedback is uncertain and will be explored in future work.

**Key words:** galaxies: formation – galaxies: evolution – galaxies: high-redshift – galaxies: star formation – galaxies:haloes

## 1 INTRODUCTION

Galaxies in the nearby Universe have a bimodal distribution of their colours (e.g., [Strateva et al. 2001](#); [Blanton et al. 2003](#); [Baldry et al. 2004](#)) and stellar age indicators ([Kauffmann et al. 2003](#); [Thomas et al. 2010](#)). The two peaks correspond to star forming galaxies (or ‘blue cloud’ or ‘main sequence’ galaxies) and quiescent galaxies (or ‘red sequence’ galaxies), respectively. The former include galaxies with blue colours, young stellar ages, and high sSFRs (e.g., [Brinchmann et al. 2004](#)). Most local galaxies of moderately low to intermediate mass ( $M_{\text{star}} \sim 10^8 - 10^{10} M_{\odot}$ ) belong to this class (e.g. [Yang et al. 2009](#); [Peng et al. 2010](#)). The second class

of galaxies, quiescent galaxies, form stars at low rates, have red optical colours, light-averaged stellar ages well in excess of 3 Gyr ([Thomas et al. 2010](#)), and dominate the massive end of the stellar mass function.

Star forming and quiescent galaxies are observed across cosmic time out to  $z \sim 3$  (e.g., [Marchesini et al. 2014](#); [Tomczak et al. 2014](#); [Man et al. 2016](#); [Martis et al. 2016](#)), or perhaps even  $z \sim 4$  ([Muzzin et al. 2013b](#); [Straatman et al. 2014](#)). Interestingly, while local massive galaxies are typically quiescent, star forming galaxies make up a large fraction ( $\sim 30 - 50\%$ ) of the massive galaxy population at  $z \sim 1.5 - 2.5$  ([Brammer et al. 2011](#); [Muzzin et al. 2013b](#); [Tomczak et al. 2014](#); [Martis et al. 2016](#)). However, these high redshift galaxies differ from their low redshift counterparts in many ways. For instance, star forming galaxies at  $z \gtrsim 1$  have an or-

\* E-mail: feldmann@physik.uzh.ch (RF)

der of magnitude higher SFR per unit stellar mass than local galaxies (e.g. Noeske et al. 2007; Daddi et al. 2007; Magdis et al. 2010; Reddy et al. 2012; Pannella et al. 2015), are more gas-rich (Daddi et al. 2010; Tacconi et al. 2013; Saintonge et al. 2013; Scoville et al. 2016; Aravena et al. 2016; Seko et al. 2016), and are smaller at fixed stellar mass (e.g., Williams et al. 2010; van der Wel et al. 2014a). Quiescent galaxies at high redshift are even more compact than their low redshift counterparts (e.g., Daddi et al. 2005; Trujillo et al. 2006; Bezanson et al. 2009; Damjanov et al. 2011; Conselice 2014; van der Wel et al. 2014a; van Dokkum et al. 2015), signifying that, at late times, such galaxies either grow substantially (e.g. via minor merging; Naab et al. 2007, 2009; Bezanson et al. 2009; Feldmann et al. 2010; Oser et al. 2010; Wellons et al. 2016) or that large galaxies preferentially join the quiescent population (e.g., Valentini et al. 2010; Carollo et al. 2013).

The presence of massive, quiescent galaxies at early times poses a serious challenge for theoretical models. At present, there is no consensus on how star formation in these galaxies is suppressed, although various suggestions abound in the literature. The responsible processes may differ depending on galaxy type (e.g., central vs. satellite galaxies), environment (e.g., field vs. cluster), and redshift, thus complicating the analysis.

A popular quenching scenario ties the formation of quiescent galaxies to feedback from active galactic nuclei perhaps connected to galaxy mergers (AGN; Di Matteo et al. 2005; Springel et al. 2005; Hopkins et al. 2006, 2008; Choi et al. 2014). Large box cosmological simulations with different models for AGN feedback are able to reproduce the massive end of the observed stellar mass function and result in a large fraction of massive, quiescent galaxies at  $z \lesssim 1$  (Vogelsberger et al. 2014; Schaye et al. 2015; Trayford et al. 2016). Although promising, the modelling of AGN feedback in cosmological simulations is clearly still in its beginning. Furthermore, various problems matching the observations remain (e.g., Ragone-Figueroa et al. 2013; Hahn et al. 2015) and evidence for a causal connection between morphological change, AGN feedback, and quenching is difficult to interpret (e.g., Alexander & Hickox 2012; Fabian 2012; Kormendy & Ho 2013).

Aside from AGN feedback a number of other physical processes have been suggested to play a role in reducing the star formation activity of massive galaxies. These include the formation of a hot gas atmosphere around massive galaxies ('halo quenching', Keres et al. 2005; Dekel & Birnboim 2006; Cattaneo et al. 2006; Gabor & Davé 2012), with long-term maintenance possibly aided by AGN feedback coupled to the hot gas (Dekel & Birnboim 2006); a reduced accretion rate onto haloes ('cosmological starvation', Feldmann & Mayer 2015; Feldmann et al. 2016); or star formation and stellar feedback driven gas depletion (e.g., 'wet compaction', Dekel & Burkert 2014; Tacchella et al. 2016). In addition, processes specific to dense environments may affect predominantly satellite galaxies, such as ram-pressure stripping of the cold ISM (Gunn & Gott 1972; Abadi et al. 1999; Cen 2014; Bahe & McCarthy 2015), stripping of the tenuous hot atmosphere ('starvation', Larson et al. 1980; Balogh et al. 2000; Kawata & Mulchaey 2008; McCarthy et al. 2008; Van Den Bosch et al. 2008; Feldmann et al. 2011; Bahe et al. 2013), and frequent tidal interactions with members of galaxy groups and clusters ('harassment', Farouki & Shapiro 1981; Moore et al. 1996).

Numerical simulations are a valuable tool to decipher how star forming galaxies transform into quiescent ones (e.g. see Somerville & Davé 2015 for a recent review). In simulations, the evolution of individual galaxies and their properties can be directly traced across cosmic time. Furthermore, it is straightforward to analyse the prop-

erties of separate galaxy populations, e.g., centrals and satellites. Of course, simulations come with their own challenges. In particular, the large dynamic range of the physical processes involved in galaxy formation requires the use of sub-grid models and introduces systematic uncertainties. It is thus important to cross-validate simulations against available observations. Fortunately, state-of-the-art hydrodynamical simulations reproduce many properties of observed galaxies thanks to efforts in modelling stellar feedback more accurately and increasing numerical resolution (e.g., Feldmann et al. 2010; Guedes et al. 2011; Hopkins et al. 2011; Agertz et al. 2013; Hopkins et al. 2014; Ceverino et al. 2015).

Theoretical models predict that star formation in galaxies (especially at higher redshift) is largely driven by the accretion of gas from the intergalactic medium (e.g., Keres et al. 2005; Dekel et al. 2009; Bouché et al. 2010; Davé et al. 2012; Feldmann 2013; Lilly et al. 2013; Sánchez Almeida et al. 2014; Schaye et al. 2015). Stellar feedback has been shown to change the shape of the star formation histories of galaxies (shifting star formation to later times and increasing variability, e.g., Schaye et al. 2010; Hopkins et al. 2014) and to disrupt the tight relation between galaxy growth and halo growth (van de Voort et al. 2011; Faucher-Giguère et al. 2011). However, the qualitative trend remains that - all else being equal - faster growing haloes harbour faster growing galaxies (Rodríguez-Puebla et al. 2016; Feldmann et al. 2016). A link between star formation and halo growth would offer a physical explanation for the empirical correlation between galaxy colours and halo formation time assumed in age-matching (Hearin & Watson 2013). However, it does not by itself explain the bimodal sSFR distribution.

In this paper, we analyse properties related to star formation, including sSFRs, stellar masses, and galaxy colours from a new sample of massive galaxies (MASSIVEFIRE; Feldmann et al. 2016) as part of the Feedback In Realistic Environments (FIRE) project<sup>1</sup> (Hopkins et al. 2014). In particular, we aim to quantify the differences between star forming and quiescent galaxies of moderate mass ( $\sim 10^{10} - 10^{11} M_{\odot}$ ) at the cosmic noon ( $z \sim 2$ ). The simulations presented in this paper are run with the same code, adopt the identical physics modelling, and use a similar resolution as the simulations reported in Hopkins et al. (2014) and Faucher-Giguère et al. (2015) but target galaxies residing in massive haloes at  $z \sim 2$ .

The FIRE approach of modelling galactic star formation and stellar feedback has been validated against observational data in a number of publications. The tests include the stellar-to-halo-mass relation (SHMR; Hopkins et al. 2014) and the stellar mass – metallicity relation (Ma et al. 2016) of  $\leq L_{*}$  galaxies at  $z = 0$  and their high redshift progenitors. Other checks include the H I content of galaxy haloes at both low and high redshifts (Faucher-Giguère et al. 2015; Faucher-Giguère et al. 2016; Hafen et al. 2016), the properties of sub-millimetre galaxies (Narayanan et al. 2015), the formation of giant star forming clumps in  $z \sim 1 - 2$  gas rich disks (Oklopčić et al. 2016), and the X-ray and S-Z signals arising from the hot gas haloes surrounding massive galaxies (van de Voort et al. 2016). We note that none of the simulations used in these works include AGN feedback. This is an intentional choice since it enables us to identify which aspects of the observed galaxy population can be understood using stellar physics alone.

The outline of this paper is as follows. The details of the simulation suite, including the set-up, sample selection, and post-

<sup>1</sup> See the FIRE project web site at: <http://fire.northwestern.edu>.

processing are introduced in §2. The subsequent sections discuss the colours of massive galaxies at  $z \sim 1.7 - 4$  and the different pathways to suppressing star formation (§3.1), the importance of dust extinction (§3.2), the stellar mass – SFR relation (§3.3), the role of the environment (§3.5), and the relation between stellar and halo mass (§3.6). We summarise our findings and conclude in the final section.

## 2 METHODOLOGY

### 2.1 Setup of the simulations

We created initial conditions for MASSIVEFIRE with the multi-scale initial conditions tool MUSIC (Hahn & Abel 2011). Our sample is drawn from a  $(144 \text{ Mpc})^3$  comoving box with  $\Omega_{\text{matter}} = 0.2821$ ,  $\Omega_{\Lambda} = 1 - \Omega_{\text{matter}} = 0.7179$ ,  $\sigma_8 = 0.817$ ,  $n_s = 0.9646$ , and  $H_0 = 69.7 \text{ km s}^{-1} \text{ Mpc}^{-1}$  (Hinshaw et al. 2013).

From a low-resolution DM only run, we select isolated haloes that fall into the following three mass bins at  $z = 2$ : (i)  $2.5 - 3.6 \times 10^{12} M_{\odot}$ , (ii)  $0.9 - 1.1 \times 10^{13} M_{\odot}$ , and (iii)  $2.5 - 3.6 \times 10^{13} M_{\odot}$ . For each such halo, we compute the mass contained within a radius of 1.8 proper Mpc as a measure of local environmental density. For the low (intermediate) mass bin, we select a total of 10 (5) haloes, two haloes (one halo) each from the 5, 25, 50, 75, and 95th percentile of the distribution of local environmental densities. For the most massive bin we select 3 haloes, one each from the 5, 50, and 95th percentile. Overall, we thus select 18 ‘primary’ haloes in 3 narrow mass ranges and with a variety of local environmental densities. No other selection criteria are used. We show the evolution of virial masses and environmental overdensities for the selected haloes in Fig 1.

Initial conditions for our ‘zoom-in’ runs follow the standard procedure from Hahn & Abel (2011) with a convex hull surrounding all particles within  $3 \times R_{\text{vir}}$  at  $z = 2$  of the chosen halo defining the Lagrangian high-resolution region.

The particle masses at the default high resolution (HR) are  $m_{\text{DM}} = 1.7 \times 10^5 M_{\odot}$  and  $m_{\text{gas}} = 3.3 \times 10^4 M_{\odot}$ , respectively. Star particles that form during a simulation have a mass equal to the gas particle they are spawned from. Masses are eight times larger at medium resolution (MR). The gravitational softening lengths for DM and star particles are fixed at 143 parsec (pc) and 21 pc (physical), respectively, for both HR and MR runs. The gravitational softening lengths for gas particles are adaptive and reach a minimum value of 9 pc in the dense interstellar medium. When weighted by instantaneous SFR, the gas softening lengths in our simulation volumes average to about 30 pc.

The MASSIVEFIRE simulation suite is summarised in Table 1. The full name of each simulation reported here is MFz2\_SeriesNumber, with Series being one of A, B, C, or Cm and Number ranging from 1 to the number of runs in each series. In the remainder of this paper we use the short form SeriesNumber to denote the runs.

### 2.2 Modelling of physical processes

All simulations here use the identical *Feedback In Realistic Environments* (FIRE) source code, physics, and parameters from Hopkins et al. (2014). This is the same code used in the FIRE simulations published in previous work (Hopkins et al. 2014; Oñorbe et al. 2015; Chan et al. 2015; Faucher-Giguere et al. 2015; Feldmann et al. 2016).

For convenience, we briefly review the most important details of the simulations. The simulations are run with the gravity-hydrodynamics code GIZMO<sup>2</sup> (Hopkins 2015), in Pressure-energy Smoothed Particle Hydrodynamics (P-SPH) mode, an improved SPH method which conserves energy, entropy, momentum and overcomes some of the problems of traditional SPH methods related to fluid mixing instabilities (Agertz et al. 2007; Hopkins 2013). It also includes improved treatments of artificial viscosity (Cullen & Dehnen 2010), conductivity (Price 2008), and higher-order kernels (Dehnen & Aly 2012).

Gas cools according to the combination of free-free, photo-ionisation/recombination, Compton, photo-electric, metal-line, molecular, and fine-structure processes, calculated from  $10 - 10^{10} \text{ K}$ , and self-consistently accounting for 11 separately tracked species (H, He, C, N, O, Ne, Mg, Si, S, Ca, Fe) each with their own yield tables directly associated with the different stellar mass return mechanisms below. Star formation occurs according to a sink-particle prescription, only in self-gravitating, dense, self-shielding molecular gas. Specifically, gas which is locally self-gravitating (according to the automatically adaptive criterion developed in Hopkins et al. (2013) from simulations of star-forming regions) and has density in excess of  $n > 5 \text{ cm}^{-3}$ , is assigned a SFR  $\dot{\rho} = f_{\text{mol}} \rho / t_{\text{ff}}$  where  $t_{\text{ff}}$  is the free-fall time and  $f_{\text{mol}}$  is the self-shielding molecular fraction calculated following (Krumholz & Gnedin 2011). As shown in several previous papers (Hopkins et al. 2013, 2014), stellar feedback leads naturally to a self-regulating SF efficiency of  $\sim 1\%$  per free-fall time in both dense gas and on galaxy scales. Note that, because of the self-gravity criterion, the mean density at which star formation occurs is much higher ( $\sim 100 \text{ cm}^{-3}$  for the resolution adopted in this work).

Once formed, each star particle acts as a single stellar population with given mass, metallicity, and age; all relevant feedback quantities are directly tabulated as a function of time from the stellar population models in STARBURST99 with a Kroupa IMF (Leitherer et al. 1999), without subsequent adjustment or fine-tuning. The simulations include several different stellar feedback mechanisms, including (1) local and long-range momentum flux from radiative pressure, (2) energy, momentum, mass and metal injection from SNe and stellar winds, and (3) photo-ionisation and photo-electric heating. We follow Wiersma et al. (2009) and include mass recycling from Type-II SNe, Type-Ia SNe, and stellar winds.

### 2.3 Sample selection

From each simulation, we analysed about 45 snapshots evenly spaced in cosmic time between  $z = 10$  to  $z = 1.7$ . We identified haloes and their dark matter (DM), gas, and stellar content with the help of the Amiga Halo Finder (AHF; Gill et al. 2004; Knollmann & Knebe 2009). We selected haloes that, at simulation redshift  $z = 2.5$ , (i) are isolated, (ii) harbour a stellar component exceeding  $10^{10} M_{\odot}$  within  $R_{\text{halo}}$ , and (iii) are not significantly contaminated with lower resolution DM particles (less than 1% by mass). Each selected halo was followed forward and backward in time by linking it to its most massive progenitor and descendent halo from the previous and next snapshot, respectively.

Our selection resulted in 37 haloes that host galaxies with stellar masses ranging from  $\sim 10^{10} M_{\odot}$  to  $\sim 5 \times 10^{11} M_{\odot}$  at  $z = 2$ . Of the selected haloes, 21 are isolated at the final snapshot, while

<sup>2</sup> A public version of GIZMO is available at <http://www.tapir.caltech.edu/~phopkins/Site/GIZMO.html>

Name of series	Number of runs	$M_{180m}(z=2)$ ( $\log_{10} M_{\odot}$ )	$z_{\text{end}}$	resolution	$m_{\text{gas}}$ ( $M_{\odot}$ )	$m_{\text{DM}}$ ( $M_{\odot}$ )	$\epsilon_{\text{gas}}$ (pc)	$\epsilon_{\text{star}}$ (pc)	$\epsilon_{\text{DM}}$ (pc)
A	10	12.5	1.7	HR	$3.3 \times 10^4$	$1.7 \times 10^5$	9	21	143
B	5	13.0	1.7	HR	$3.3 \times 10^4$	$1.7 \times 10^5$	9	21	143
C	1	13.5	2	HR	$3.3 \times 10^4$	$1.7 \times 10^5$	9	21	143
Cm	2	13.5	1.7, 2	MR	$2.7 \times 10^5$	$1.4 \times 10^6$	9	21	143

**Table 1.** *Simulations in this paper.* The simulations are grouped into series A, B, C, and Cm (first column). The number of runs in each series is listed in the second column and subsequent columns offer additional information about each series. The third column lists the mass of the targeted, primary halo in a given run. Column 4 reports the redshift at which the simulation is stopped. Column 5 through 10 list the numerical resolution. Columns 6 and 7 state the mass resolution of gas and dark matter particles, while columns 8 through 10 list the gravitational softening lengths for gas, star, and dark matter particles (the gas softening is fully adaptive and the minimal softening length is quoted). All MASSIVEFIRE runs use identical FIRE code and physics (Hopkins et al. 2014).

Name	Central/Satellite	$\log_{10} M_{180m}$ ( $\log_{10} M_{\odot}$ )	$R_{\text{halo}}$ (kpc)	$\log_{10} M_{\text{star}}$ ( $\log_{10} M_{\odot}$ )	SFR ( $M_{\odot} \text{ yr}^{-1}$ )	$\log_{10} \text{sSFR}$ ( $\log_{10} \text{ yr}^{-1}$ )	U-V (mag)	V-J (mag)	$f_Q$ (%)
A1:0	Central	12.38	144.3	10.40	12.5	-9.19	1.205	0.711	2
A2:0	Central	12.48	156.0	10.54	13.6	-9.23	1.316	0.849	4
A3:0	Central	12.38	144.9	10.04	6.4	-9.18	1.037	0.690	0
A4:0	Central	12.46	153.5	10.33	6.2	-9.24	1.242	0.632	98
A5:0	Central	12.38	144.6	10.25	14.3	-8.90	0.951	0.271	2
A6:0	Central	12.44	151.9	10.41	0.6	-10.43	1.488	0.742	100
A7:0	Central	12.41	148.7	10.29	1.2	-9.80	1.246	0.529	60
A8:0	Central	12.56	166.4	10.08	0.2	-9.98	1.183	0.409	40
A9:0	Central	12.48	156.6	10.00	0.1	-11.09	1.269	0.420	100
A9:1	Central	12.16	122.6	10.23	3.8	-9.45	1.330	0.857	52
A10:0	Central	12.53	162.4	10.43	6.8	-9.30	0.984	0.262	8
B1:0	Central	12.93	221.0	10.91	30.5	-9.19	1.246	0.819	0
B2:0	Central	12.97	227.5	10.88	0.8	-10.77	1.406	0.585	100
B3:0	Central	13.00	232.6	10.83	12.3	-9.41	1.073	0.630	0
B3:1	Satellite	11.54	30.1	9.75	3.4	-9.33	0.925	0.179	0
B4:0	Central	12.94	222.6	10.55	61.3	-8.39	0.626	0.120	0
B4:1	Central	12.25	130.6	9.78	0.4	-9.82	1.164	0.282	30
B4:2	Central	12.06	113.0	10.03	0.3	-10.37	1.280	0.536	100
B4:3	Satellite	12.03	70.7	10.11	13.2	-8.90	1.188	0.757	14
B5:0	Central	12.97	227.8	10.75	22.8	-9.13	1.368	1.010	0
B5:1	Satellite	11.41	39.1	9.84	0.0	-12.57	1.411	0.477	100
Cm1:0	Central	13.45	330.1	11.73	160.6	-9.36	1.117	0.543	4
Cm1:1	Satellite	11.55	75.2	10.01	25.6	-8.57	0.890	0.331	0
C2:0	Central	13.42	321.4	11.14	11.1	-9.38	0.992	0.548	0
C2:1	Satellite	11.91	24.8	10.17	51.3	-8.78	0.876	0.499	0
C2:2	Satellite	12.08	50.6	10.36	22.8	-9.00	1.165	0.633	18
C2:3	Satellite	11.31	30.7	9.81	0.0	-13.33	1.259	0.295	96
Cm3:0	Central	13.46	331.8	11.38	183.8	-8.98	1.140	0.606	8
Cm3:1	Central	12.99	231.8	11.24	153.6	-8.90	1.297	0.802	48
Cm3:2	Satellite	12.73	75.7	10.96	55.3	-9.16	1.247	0.656	90
Cm3:3	Central	12.13	119.5	10.35	47.2	-8.57	0.973	0.678	0
Cm3:4	Satellite	11.95	89.7	10.52	37.7	-8.90	1.227	0.915	0
Cm3:5	Central	11.91	100.8	10.19	32.0	-8.62	1.069	0.934	0
Cm3:6	Satellite	11.83	95.0	10.15	31.5	-8.39	0.822	0.095	0
Cm3:7	Central	11.67	84.0	9.94	0.4	-10.26	1.136	0.251	30
Cm3:8	Satellite	11.50	34.9	10.22	27.2	-8.82	1.064	0.569	0
Cm3:9	Satellite	11.47	26.1	10.16	20.3	-8.97	1.099	0.765	0
Cm3:10	Satellite	11.04	15.4	10.00	0.2	-10.80	1.090	0.243	4

**Table 2.** *Properties of simulated galaxies at  $z = 2$ .* The name of the galaxy is provided in the first column. The next column shows whether the galaxy is a central or a satellite galaxy at this redshift. Columns 4 and 5 provide the logarithm of the halo mass and the halo radius, respectively. Columns 6 lists the stellar mass within  $0.1 R_{\text{halo}}$ . Column 7 and 8 report the SFR and the logarithm of the sSFR within 5 kpc. The next two columns list the median (for 50 random lines of sight) rest-frame U-V and V-J colours. The galaxy would be classified as quiescent according to a colour-colour criterion (Whitaker et al. 2011) for the fraction of random lines of sight provided in the last column.

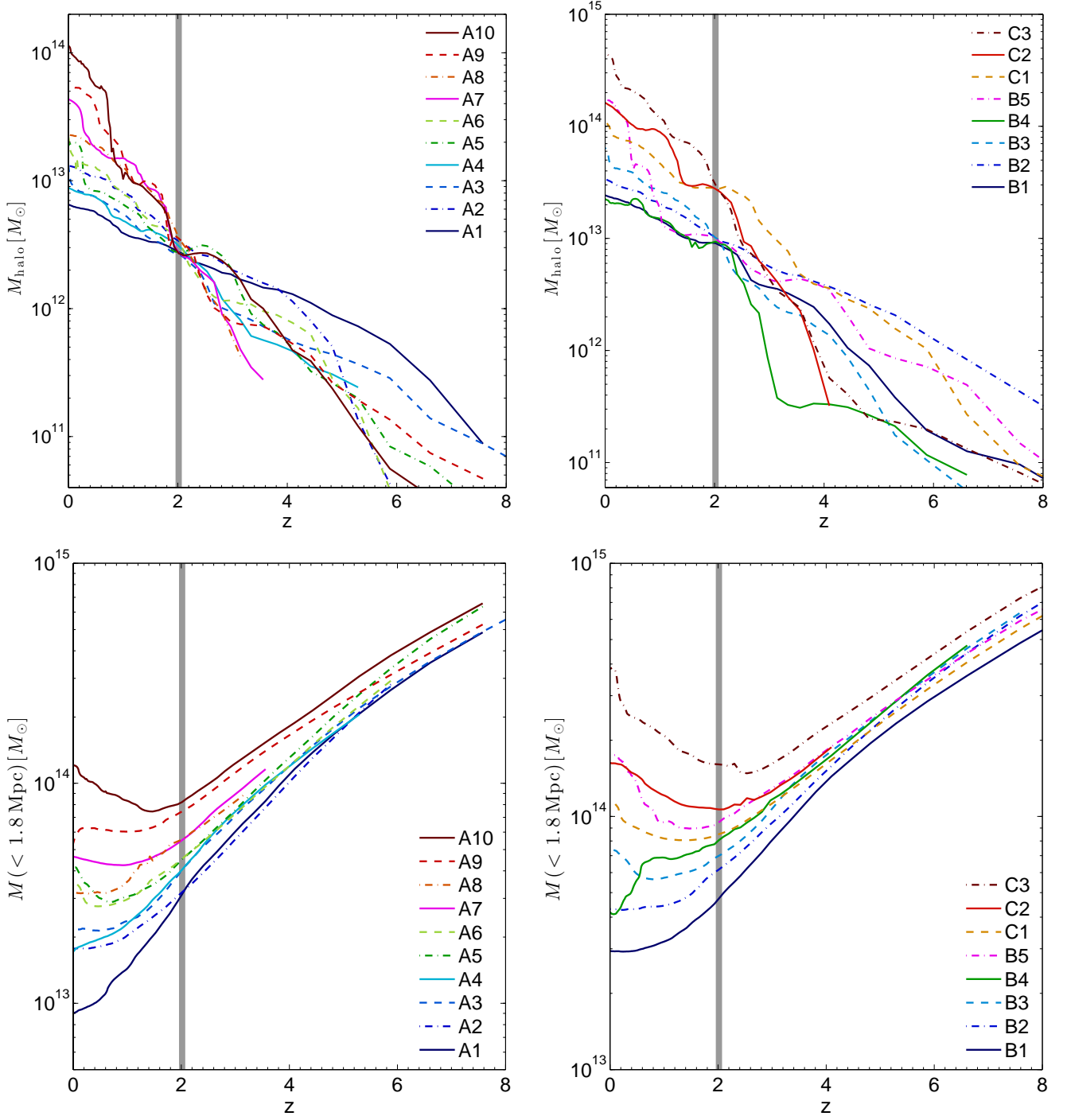


**Figure 1.** Redshift evolution of halo mass (top panels) and local overdensity (bottom panels) of the haloes selected by this study based on a lower resolution  $N$ -body simulation. The masses of the selected haloes at  $z = 2$  fall into one of the following ranges:  $2.5 - 3.6 \times 10^{12} M_{\odot}$  (top left panel, series A),  $0.8 - 1.2 \times 10^{13} M_{\odot}$  (lower 5 lines at  $z = 2$  in the top right panel, series B), or  $2.5 - 3.6 \times 10^{13} M_{\odot}$  (upper 3 lines at  $z = 2$  in the top right panel, series C). The grey band in each panel indicates the selection redshift  $z = 2$ . From each mass bin we select haloes from low, medium, and high density environments, with no other selection criteria. The simulations reported here span a large range of halo growth histories and environmental densities.

16 are sub-haloes. In other words, 21 of the 37 selected massive galaxies are centrals and 16 are satellite galaxies. Each zoom-in region also contains a large number of lower mass ( $M_* < 10^{10} M_{\odot}$ ) galaxies. These galaxies are not the focus of this work and their properties are discussed elsewhere (e.g., Sparre et al. 2016). We

list global properties of the selected MASSIVEFIRE galaxies and their haloes at  $z = 2$  in Table 2 and at  $z = 1.7$  in the Appendix.



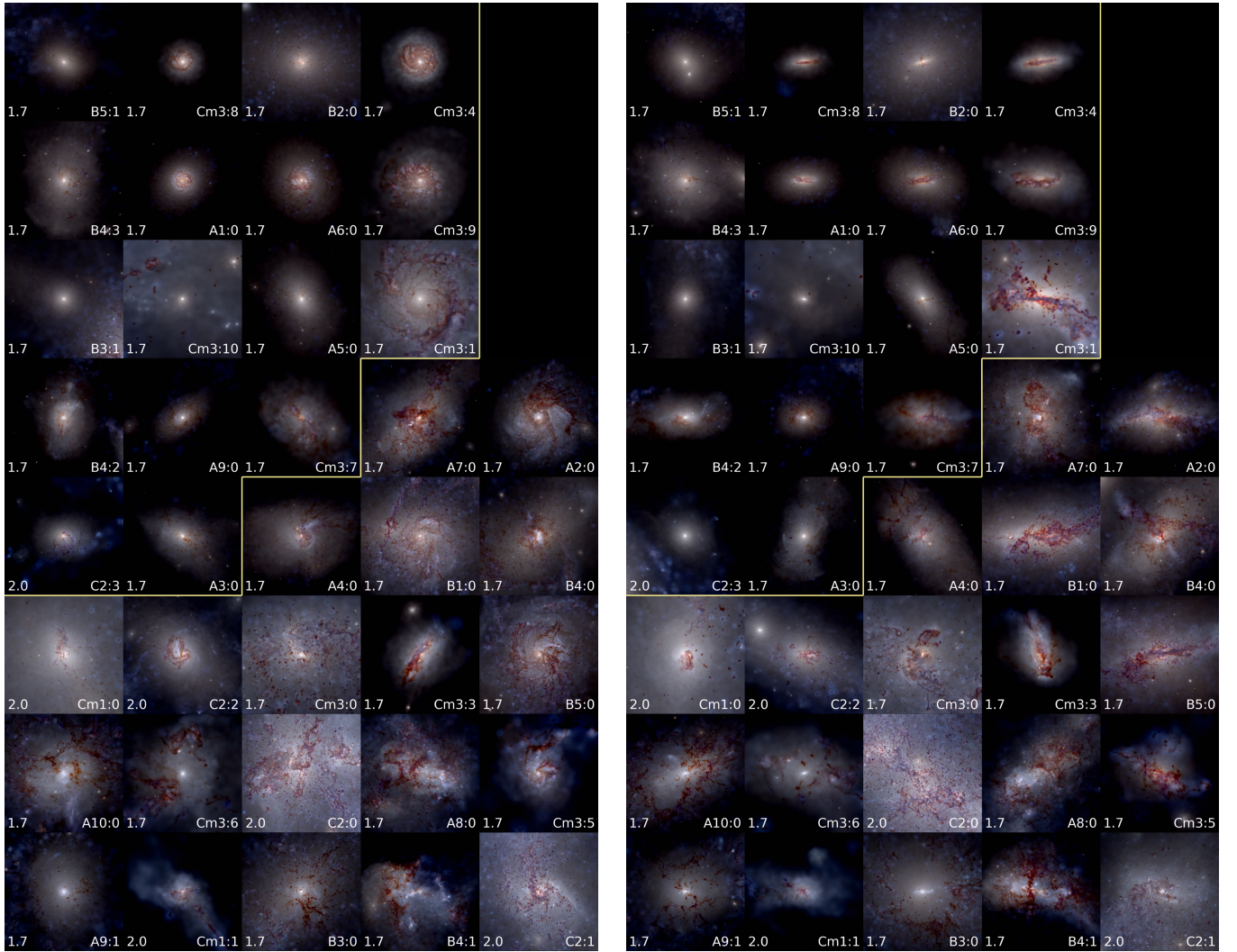


**Figure 2.** Restframe U, V, J band composite images of the  $z \sim 2$  MASSIVEFIRE galaxies. We show face-on (left) and edge-on (right) projections for the final snapshot (i.e., either  $z = 2$  or  $z = 1.7$ ) of each galaxy. The image stamps are ordered according to their rest-frame V–J (x-axis) and U–V (y-axis) colours as described in the text. The yellow boundary separates galaxies classified as quiescent and star forming, respectively, based on the (Whitaker et al. 2011) criterion. Each image stamp has a size of  $30 \times 30 \text{ kpc}^2$  centred on the target galaxy and shows rest-frame U, V, and J surface brightness mapped to blue, green, and red channels with the same normalisation relative to the Sun and with a fixed dynamic range of 1000. Our sample includes galaxies with a large variety of morphologies, including large star forming disk galaxies (e.g., the galaxy in the 5th row, 4th column), massive, quiescent early-type galaxies (e.g., the galaxy in the top row, 3rd column), and irregular, star forming galaxies (e.g., the galaxy in the bottom row, 4th column).

## 2.4 Postprocessing

**Masses and SFRs:** The stellar mass of each galaxy is defined as the stellar mass within a sphere of radius  $0.1 R_{\text{halo}}$  centred on the galaxy. We mask the contribution of satellite galaxies by subtracting the stellar mass contained within sub-haloes located at a distance  $2 \text{ kpc} \leq r \leq R_{\text{halo}}$  from the centre of the parent halo. In a few cases (during major mergers), this removal reduces the stellar mass within  $0.1 R_{\text{halo}}$  by up to 50%, but typically the correction is small. We measure SFRs and specific SFRs in 5 kpc radii to approximately mimic aperture based flux measurements (Whitaker et al. 2011; Schreiber et al. 2015). Gas masses are also measured with 5 kpc radii and include all gas phases. The SFR is computed as the average number of stars formed within the past  $10^8$  years unless specified otherwise.

**Measurements of environment:** The local environmental density of a galaxy is defined as the average density within a spherical shell with boundaries at  $R = R_{\text{halo}}$  and  $R = 5 R_{\text{halo}}$ . Compared with the definition used to select haloes (§2.1) the mass of the parent halo of the galaxy is excluded and, thus, does not affect the estimate of the environmental density. Furthermore, by defining the local environment in terms of  $R_{\text{halo}}$ , we can compare the value of the environmental density for haloes with very different masses. In particular, if haloes of different masses were completely self-similar with identical radial density profile out to  $5 R_{\text{halo}}$  then the definition above would return the same environmental density for each of them. We use the Hill radius of the halo of a galaxy as a second measure of environment. The Hill radius quantifies the extent of the gravitational sphere of influence of a halo in the presence of external perturbing bodies. We compute the Hill radius of halo  $j$  with mass  $M_j$  based on the approximate for-

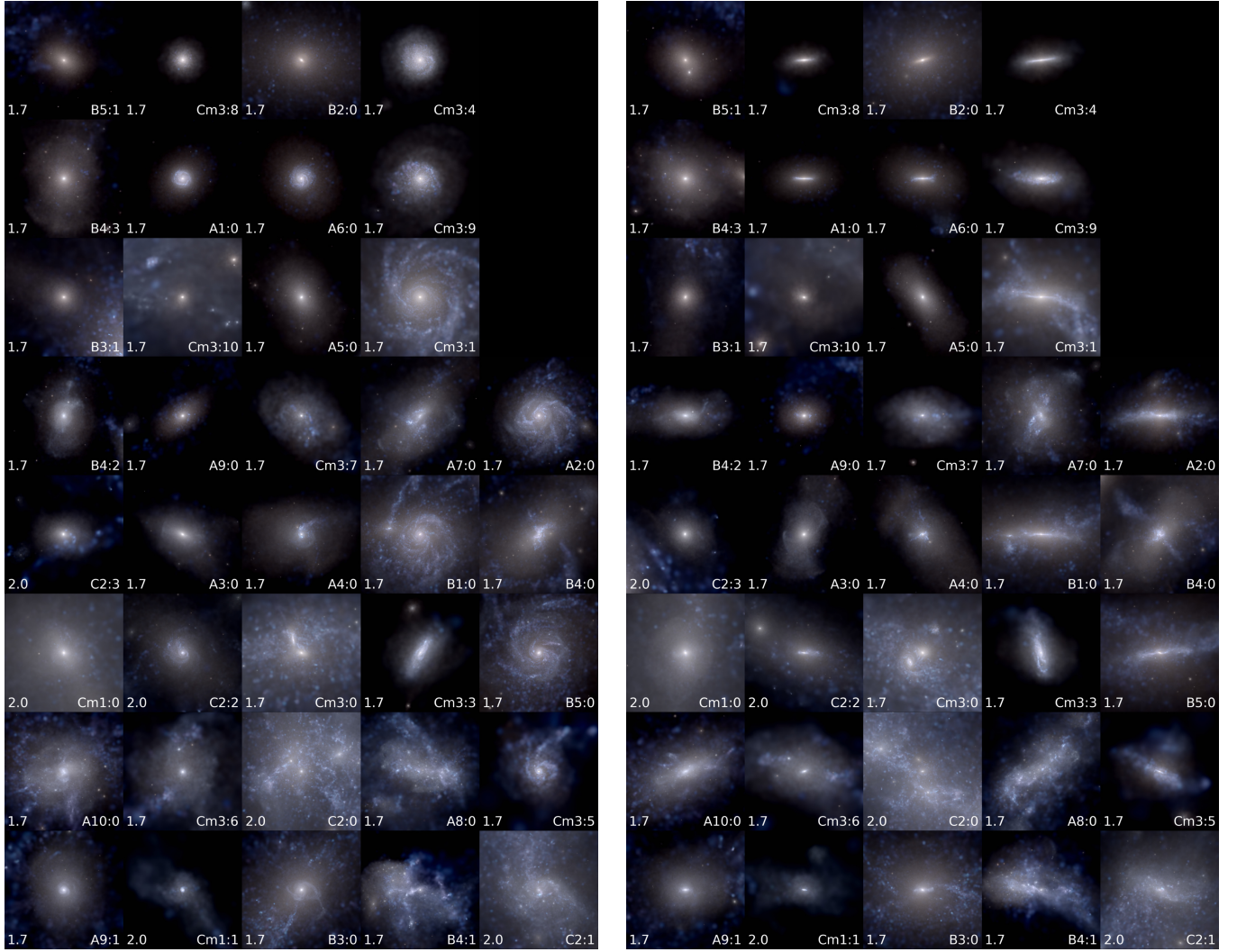


**Figure 3.** Restframe U, V, J band images as in Fig. 2 but without dust (panel ordering is the same). Visual inspection reveals that  $\sim 1/3$  of the galaxies in our sample harbor an extended disk of young stars.

mula  $R_{\text{Hill},j} = \min_{i \neq j} R_i [M_j / (3M_i)]^{1/3}$ , where  $R_i$  is the proper distance (between halo centres) to an isolated halo  $i$  of mass  $M_i$ . Haloes  $i$  with  $M_i < M_j/3$  lie inside the Hill sphere they produce and are excluded from the analysis.

**Galaxy colours and images:** We obtain images and fluxes in the rest-frame Johnson U, V, and Cousins J broad-bands by ray-tracing the light emission from stellar particles and including the attenuation by intervening dust, but not scattering, following Hopkins et al. (2014). Each stellar particle is treated as a single stellar population of given age, mass, and metallicity. We use the isochrone synthesis model by Bruzual & Charlot (2003) with Padova stellar tracks to compute the luminosities of star particles in each band. The initial stellar mass function (Chabrier 2003) has lower and upper cut-off masses of  $0.1 M_\odot$  and  $100 M_\odot$ , respectively. The dust opacity in each band is computed for an SMC dust composition (Pei 1992), scaled linearly with the metallicity of the gas ( $Z$ ) and normalised such that the optical depth in the Johnson B band is 0.78 for a  $10^{21} \text{ cm}^{-2}$  column of hydrogen atoms with  $Z = 0.02$  (Pei 1992). U-V and V-J colours are measured within (projected) circular apertures

of 5 kpc radius centred on each galaxy with the contribution from satellite galaxies masked.

**Growth rates:** Growth rates at  $z \sim 2$  are computed for the cold baryonic mass ( $M_{\text{bar}} = M_{\text{star}} + M_{\text{H I}} + M_{\text{H}_2}$  within  $0.1 R_{\text{halo}}$ ) of each galaxy in our sample and for the DM mass of their haloes ( $M_{\text{DM}}$ ). The procedure is briefly described in Feldmann et al. (2016) and it follows largely McBride et al. (2009).  $M_{\text{bar}}$  and  $M_{\text{DM}}$  are fitted with a modified exponential  $\propto (1+z)^\beta e^{-\gamma z}$  (Tatsiomi et al. 2004) over the redshift range  $z \sim 2 - 7$ . The specific growth rate at redshift  $z_0$  is then computed as  $d \ln M / dt = [\beta / (1 + z_0) - \gamma] dz / dt$ .

### 3 GALAXY PROPERTIES

We show composite images in rest-frame U, V, and J band filters of the MASSIVEFIRE sample at  $z \sim 1.7 - 2$  in Fig. 2. The panels are ordered according to the rest-frame U-V and V-J colours. Fig. 2 thus mimics a colour-colour diagram with quiescent galaxies at the top left and star forming galaxies at the bottom and at the right.



In particular, we first sort galaxies based on their restframe U–V colour and split them into 8 bins (from bottom to top). In each U–V bin we sort galaxies according to the restframe V–J colour (from left to right). The yellow line separates star forming from quiescent galaxies based on the criterion that a galaxy is quiescent if  $U - V > 1.2$ ,  $V - J < 1.4$ , and  $U - V > 0.88 \times (V - J) + 0.59$  (Whitaker et al. 2011).

Overall, the galaxies show a large diversity in morphologies, colours, and dust abundances. The sample includes dusty, star forming disk galaxies, dusty irregular galaxies, dust-poor early-type galaxies, and merging/interacting galaxies. Visually, the dust abundance is lower in quiescent galaxies but perhaps somewhat surprisingly many galaxies classified as quiescent contain a significant amount of dust (discussed in §3.1).

In Fig. 2, face-on (edge-on) projections<sup>3</sup> of the simulated galaxies are shown in the left (right) panels. The edge-on view reveals that many galaxies in our sample (about 1/3 of the star forming galaxies by visual inspection) have a well-defined disk component. This should be compared with observations which indicate that about 30%-80% of  $z \sim 2$  galaxies are rotation supported and/or have low Sérsic indices (Förster Schreiber et al. 2009; Jones et al. 2010; van der Wel et al. 2014b; Wisnioski et al. 2014).

Quiescent galaxies are in about equal parts centrals and satellites, while 65% of the star forming galaxies are centrals and only 35% are satellites. This difference is not unexpected as satellite galaxies may experience strong environmental forces, such as ram pressure and tidal stripping, that affect star formation. However, given our limited sample, this is not a highly significant difference ( $p = 0.14$  according to a one-tailed two proportion test).

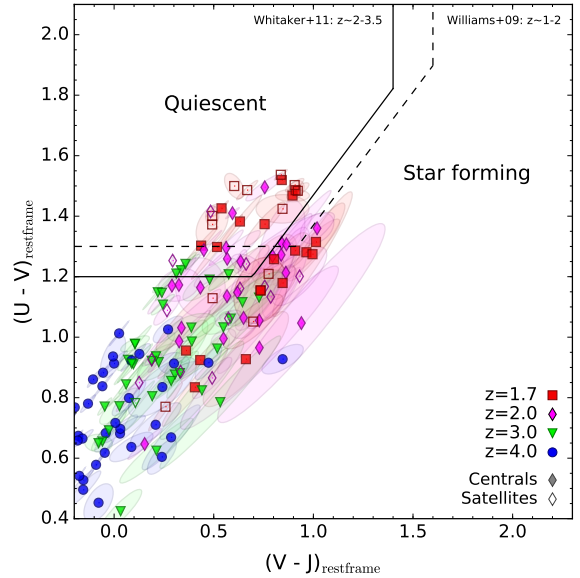
### 3.1 Galaxy colours

Fig. 3 shows dust-free images of our sample of galaxies, arranged as in Fig. 2. The edge-on views in Fig. 2 give the impression that disk galaxies have large scale heights and disturbed morphologies. However, if we remove the dust extinction we see that young stars are often arranged in a well-defined disk with a scale height significantly shallower than that of the dust. Most galaxies show the presence of an extended and more spherically distributed stellar component of older stars, but often at low surface brightness. In some cases stellar feedback is able to clear the central few kpc of a galaxy of dust and gas.

Interestingly, a small fraction of these high redshift galaxies lack a well-defined centre, e.g., B4:1, A8:0. These galaxies are typically fast growing, highly star forming galaxies with blue U–V colours.

Colour-colour diagrams have proved to be an efficient means of separating galaxies with below average sSFRs from more typical, star forming galaxies (e.g. Labbe et al. 2005; Wuyts et al. 2007; Williams et al. 2009; Whitaker et al. 2011; Brammer et al. 2011). In Fig. 4 we plot the average (over 50 random lines of sight) U–V and V–J rest-frame colours of our sample at  $z = 4, 3, 2$ , and 1.7. The figure highlights that the simulation at  $z \lesssim 2$  include both galaxies classified as quiescent and as star forming according to the empirical UVJ criterion.

<sup>3</sup> The face-on direction is defined as parallel to the angular momentum vector of star particles with an age less than 200 Myr located within 2.5 kpc from the centre of the galaxy. When necessary, we increase the maximum age in steps of 200 Myr until we end up with at least 100 such star particles.



**Figure 4.** Restframe U–V vs. V–J colours of the MASSIVEFIRE sample at  $z = 4, 3, 2$ , and 1.7. U–V and V–J colour are averaged over 50 random projections of each galaxy. Coloured ellipses show 1- $\sigma$  deviations around the mean. Filled and empty symbols distinguish central from satellite galaxies. The solid line (our adopted choice for the remainder of this paper; Whitaker et al. 2011) and the dashed line (Williams et al. 2009) are used to empirically separate quiescent galaxies from star forming galaxies.

For a more quantitative analysis, we select a subset of galaxies from the UltraVISTA survey (McCracken et al. 2012; Muzzin et al. 2013a) with similar stellar masses and redshifts. The detailed analysis is provided in Appendix A1. While the colours of the simulated and observed galaxies generally overlap, there are significant differences. In particular, unlike observations, our simulations lack galaxies with U–V rest-frame colours above 1.6. We note that the UltraVISTA catalog is not mass-complete down to  $10^{10} M_{\odot}$  at  $z = 2$  and that galaxies with  $U - V > 1.6$  are typically more massive ( $M_{\text{star}} > 10^{11} M_{\odot}$ , Williams et al. 2010). However, the mass dependence alone is unlikely to fully explain this difference. This may imply that our simulations lack an important ingredient, e.g., AGN feedback. We also note that star forming galaxies in our simulations lie, on average, somewhat closer to the star forming vs. quiescent separation line than star forming galaxies in UltraVISTA.

A bimodality in colour-colour space has been observed out to  $z \sim 2$  (e.g., Williams et al. 2009; Whitaker et al. 2011; Muzzin et al. 2013a; Martis et al. 2016), and it has been suggested that the bimodality exists at even higher redshifts (e.g., (Brammer et al. 2009; Whitaker et al. 2011; Muzzin et al. 2013a; Tomczak et al. 2014)). We compute the distance from the star forming / quiescent boundary (Whitaker et al. 2011) and test for multimodality with the dip test (Hartigan & Hartigan 1985) by selecting one line of sight for each galaxy. The dip test does not reveal evidence for a non-unimodal distribution. However, as we show quantitatively in Appendix A2, the size of our sample is too small to detect a colour bimodality with statistical significance even if one were present.

Fig. 4 also shows that galaxy colours become redder with time. This result is a consequence of two independent processes. First, galaxies with constant or declining star formation rates become redder as the stellar population ages (e.g., Wuyts et al. 2007).



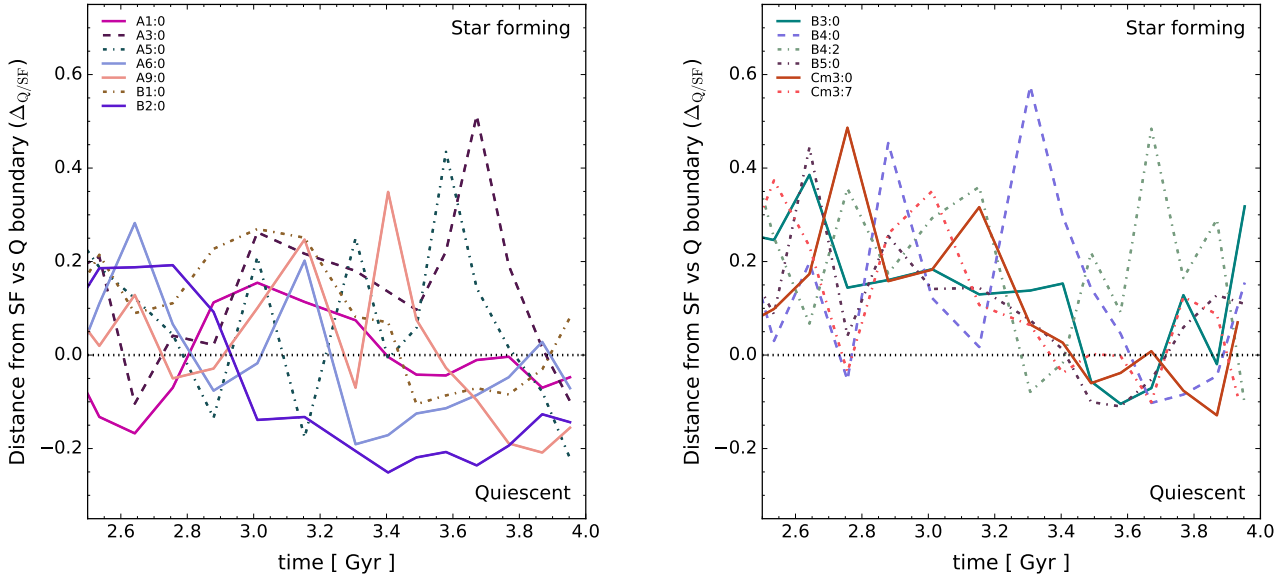


**Figure 5.** Median distance from the boundary separating star forming and quiescent galaxies in Fig. 4 as a function of time. The panels show the subset of central galaxies in our sample that spend some time in the quiescent regime. Galaxies that lie above (below) the dotted line are classified as star forming (quiescent). The time sampling is about 100 Myr, comparable to the timescale for intrinsic colour evolution. Many of our galaxies are quiescent for only a brief period of time ( $< 100$  Myr) but several remain quiescent for many hundreds of Myr.

Secondly, the dust extinction of many galaxies increases with time between  $z = 4$  and  $z = 1.7$  resulting in a diagonal shift towards redder U–V and V–J colours.

The colours of most galaxies depend on the particular line-of-sight. However, as the diagonal separation line of the UVJ criterion is approximately parallel to the dust reddening vector, the classification of galaxies into quiescent / star forming is typically much less affected by a change in viewing angle. The Euclidian distance to the separation line,  $\Delta_{Q/SF}$ , is thus a useful quantity that only weakly depends on the chosen line-of-sight for a given galaxy. Negative (positive) values of  $\Delta_{Q/SF}$  correspond to the quiescent (star forming) region of the colour–colour diagram.

Fig. 5 shows the separation from the quiescent vs. star forming boundary,  $\Delta_{Q/SF}$ , for the 13 of our 21 central galaxies that become quiescent by  $z \sim 1.7$  or that are quiescent for two or more consecutive simulation snapshots. As is clear from the figure, the quiescent / star forming classification of many galaxies varies both on long and on short time scales. Some galaxies, e.g., B2:0, become and remain quiescent for hundreds of Myr, while others, e.g., B4:2, are in the quiescent region of the UVJ colour diagram for only a brief amount of time ( $\lesssim 100$  Myr).

In Fig. 6 we compare the scatter in  $\Delta_{Q/SF}$  arising from viewing angle variations (standard deviation of  $\Delta_{Q/SF}$  over 50 random sightlines) with the scatter caused by evolutionary processes (standard deviation of  $\Delta_{Q/SF}$  sampled at 3 times separated by 100 Myr). The scatter of  $\Delta_{Q/SF}$  caused by evolutionary processes dominates the scatter caused by viewing angle variations.

Without dust, variations in colours with viewing angle are negligible, yet the variations with time remain similar. In other words, evolutionary color changes are caused by bursty star formation and not by changes in the dust distribution. For star forming galaxies, time variations of  $\Delta_{Q/SF}$  based on intrinsic colours are actually often somewhat *larger* than time variations based on dust-reddened

colours. Hence, for star forming galaxies in our sample, dust preferentially reddens regions with young stellar populations, i.e., sites of recent star formation.

To better understand the different timescales over which galaxies have colours that place them in the quiescent regime, Fig. 7 shows the sSFRs for a representative subset of the central galaxies in our sample. Specifically, we measure the sSFR of 4 galaxies (two are classified as star forming and the other two as quiescent at  $z = 1.7$  based on their U–V and V–J colours) and their main progenitors between  $z = 1.7$  and  $z = 8$ . This figure highlights a number of important results.

First, it shows that high-redshift galaxies have complex star formation histories with large amounts of short-term variability. The amount of variability is stronger for SFR estimators with shorter tracer lifetimes. In particular, the 5 Myr average sSFRs of many galaxies show bursts of a factor of a few above the star forming sequence. These short star bursts are typically followed by a strong, but short-lived ( $\lesssim 100$  Myr), suppression of the star formation activity. SFRs averaged over longer lifetimes, e.g., 100 Myr, show still a significant, albeit reduced, amount of variability. With this longer tracer, individual star forming galaxies approximately co-evolve with the star forming sequence.

Fig. 7 also clarifies the role of mergers in suppressing the star formation activity in galaxies. Specifically, we compare the stellar mass that is accreted during a given snapshot with the stellar mass of the central galaxy (all masses are measured within the central 5 kpc) at the given time, see grey bars in Fig. 7. Ratios of  $\gtrsim 1 : 4$  suggest significant merger events. We find that many of the starbursts and star formation suppression events do not coincide with major mergers. We leave a more detailed study of the triggers of starbursts in massive, high- $z$  galaxies for future work.

In Fig. 8, we directly compare how the star forming / quiescent classification based on colours relates to a division based on

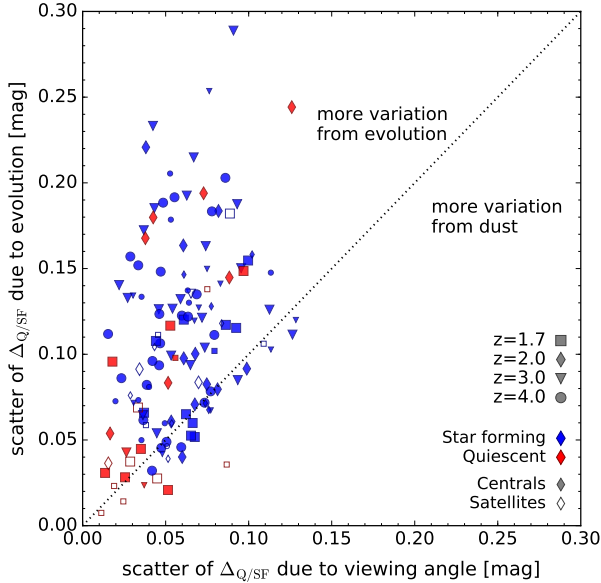


**Figure 6.** Scatter of  $\Delta_{Q/SF}$  caused by line-of-sight variations and by evolution over 100 Myr timescales. Red (blue) symbols denote lines of sight that place a given galaxy in the quiescent (star forming) part of the UVJ diagram. Large and small symbols show HR runs (series A, B, and C) and MR runs (series Cm), respectively. Evolutionary processes lead to a larger scatter of  $\Delta_{Q/SF}$  ( $\sim 0.03 - 0.25$  mag) than viewing angle variations ( $\sim 0.02 - 0.1$  mag). Evolutionary changes are linked to colour variations of the underlying stellar population while the line-of-sight variations are driven by a non-homogeneous dust distribution.

sSFRs. In particular, we show  $\Delta_{Q/SF}$  vs the sSFR offset from the star forming sequence (i.e., the locus of ‘main sequence’ galaxies). The figure demonstrates that it matters how SFRs are measured – the results are remarkably different if near instantaneous SFRs or SFRs averaged over 100 Myr are used.

The bottom panel shows our default case of averaging SFRs over 100 Myr (roughly comparable to SFRs based on FUV, Sparre et al. 2016). Quiescent galaxies have sSFRs that are a factor 4 or more below the star forming sequence. In contrast, star forming galaxies tend to have sSFRs that are at most a factor of a few above or below the star forming sequence and that are strongly correlated with  $\Delta_{Q/SF}$ .

In the top panel of Fig. 8 we show the corresponding results if near instantaneous SFRs are used (here 5 Myr averaging time; roughly comparable to SFRs based on H- $\alpha$  luminosity). In this case, the tight correlation between  $\Delta_{Q/SF}$  and the sSFR offset from the star forming sequence is almost lost. SFRs of star forming galaxies are highly variable on short timescales (see Fig. 7) resulting in slightly more than half of such galaxies having sSFRs a factor 4 or more below the star forming sequence.

In short, classifying galaxies as star forming / quiescent based on colours is roughly equivalent to a classification based on sSFRs if sufficiently long SFR averaging timescales are used.

### 3.2 Dust Extinction

Dust reddening and extinction can strongly affect the observed colours of galaxies. The ‘true’ dust extinction  $A_V$  is computed as the difference between the observed and the intrinsic rest-frame V

magnitude of a given galaxy, see §2.4. Note that we do not model dust extinction as a simple screen as we find this to overestimate (for a given fixed amount of dust mass) the reddening. Our models do not include a separate circumstellar dust component that is present in local star forming galaxies (Calzetti et al. 2000; Wild et al. 2011), and perhaps also at  $z \sim 2$  (e.g., Förster Schreiber et al. 2009; Yoshikawa et al. 2010; Kashino et al. 2013; Price et al. 2014).

In Fig. 9 we show the dust extinction of our simulated galaxies as function of stellar mass and sSFR. The level of dust extinction in our sample matches estimates for mass-complete<sup>4</sup> samples of  $z \sim 1.5 - 2$  galaxies (Bauer et al. 2011; Price et al. 2014; Mancini et al. 2015; Pannella et al. 2015; Dunlop et al. 2016). Furthermore, our simulations predict a scaling of  $A_V$  with  $M_{\text{star}}$  and with sSFR in broad agreement with observations. In particular, the amount of dust extinction increases with increasing stellar mass, with increasing SFR (not shown), and with increasing sSFR (for galaxies on and below the star forming sequence).

Some of our quiescent galaxies contain substantial dust masses. Such galaxies tend to have sSFRs that place them only somewhat below the star forming sequence, but most of their current star formation is dust-enshrouded and the stellar light is dominated by an old stellar population. We also find a significant fraction of galaxies with sSFR (averaged over 100 Myr) near the main sequence that show low amounts of extinction ( $A_V < 0.5$ ). These galaxies have actually low levels of instantaneous star formation. Dust extinction is more strongly correlated with the sSFR averaged over shorter timescales; we thus predict that an observationally derived correlation between  $A_V$  and sSFR based on tracers with long life times, e.g., FUV or IR derived estimates, will show a significant amount of scatter.

When considering different galaxy types, we find that quiescent satellites are typically the least dust obscured (the 16, 50, and 84th percentiles of  $A_V/\text{mag}$  are 0, 0.41, and 1.78, respectively), followed by quiescent centrals (0.22, 0.6, 1.55), star forming centrals (0.24, 1.14, 1.81), and then star forming satellites (0.05, 1.35, 2.17). The  $A_V$  distributions of the latter two are statistically indistinguishable (according to Kolmogorov-Smirnov and Anderson-Darling tests). This finding appears to be broadly consistent with the observation that star forming satellite galaxies in groups and clusters have similar properties as star forming galaxies of the same stellar mass in the field (e.g., Balogh et al. 2004; Park et al. 2007; Peng et al. 2010; McGee et al. 2011; Wijesinghe et al. 2012).

We see a clear trend of  $A_V$  increasing with time (the median  $A_V$  for the galaxies in our sample scales approximately as  $0.43(t/\text{Gyr}) - 0.50$ ) as both the galaxy masses and metallicities increase - broadly in agreement with observations of Lyman break galaxies at high redshift (e.g., Steidel et al. 1999; Bouwens et al. 2009).

### 3.3 The star forming sequence

SFRs of non-quiescent galaxies are positively correlated with galaxy masses (e.g., Daddi et al. 2007; Whitaker et al. 2012; Speagle et al. 2014). The relation is approximately linear over a large range in stellar masses, i.e., the sSFR is not a strong function of stellar mass, except perhaps at the high mass end. The normalisation of the stellar mass – sSFR relation evolves strongly with redshift. To

<sup>4</sup> Stellar masses reported by (Bauer et al. 2011; Mancini et al. 2015; Pannella et al. 2015) are lowered by 0.24 dex to convert from a Salpeter to a Chabrier IMF (Santini et al. 2012).

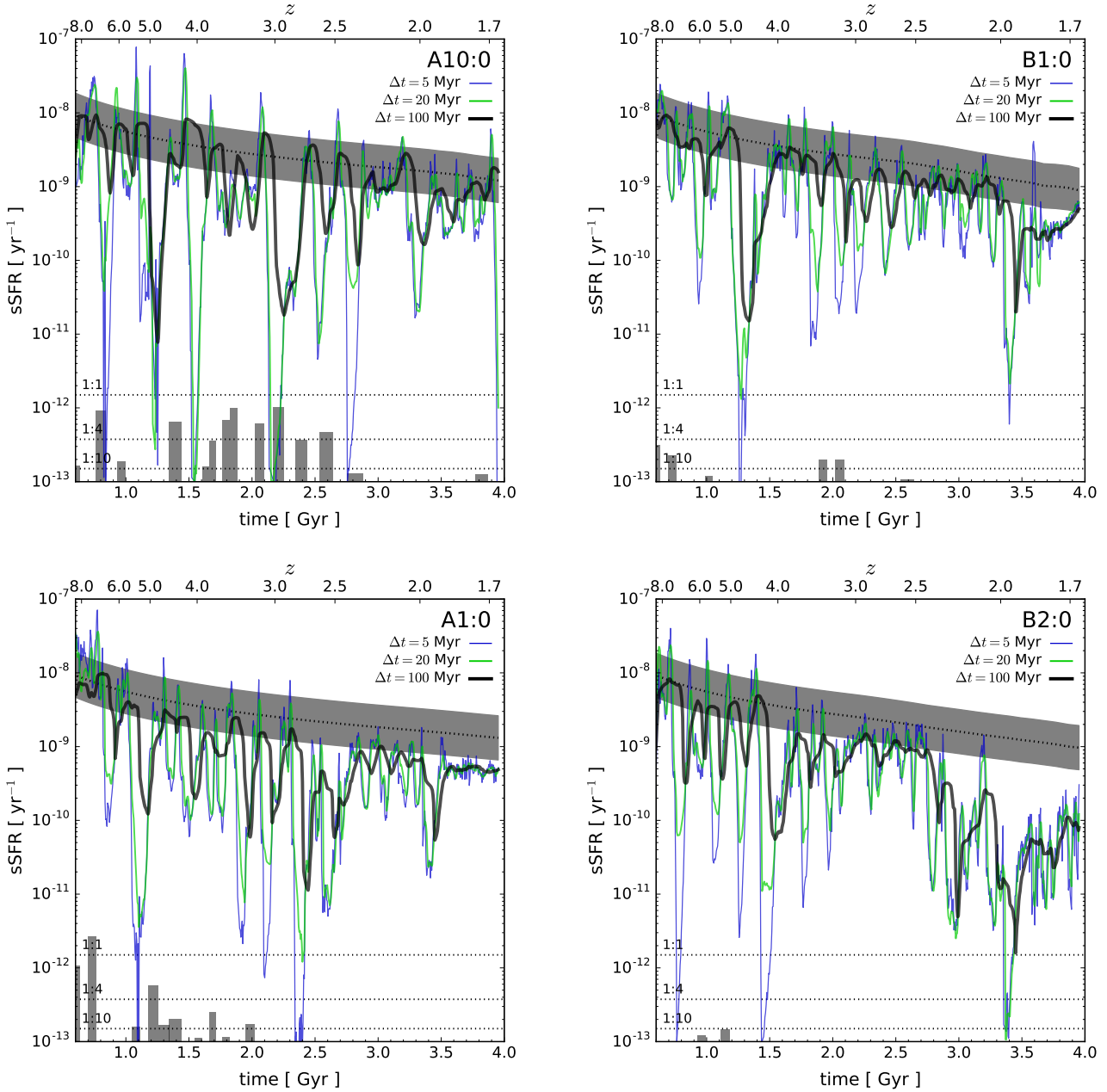


**Figure 7.** Evolution of the sSFR for galaxies classified as star forming (top row) and quiescent (bottom row) based on their  $U-V$  and  $V-J$  colours. Thick, medium-thick, and thin lines show the sSFRs averaged over the past 100 Myr, 20 Myr, and 5 Myr, respectively. Grey bands and dotted lines indicate typical sSFRs of observed star forming galaxies at comparable redshifts and with similar stellar masses (Schreiber et al. 2015). The bars at the bottom of each panel reveal how much mergers contribute to the change in stellar mass between two snapshots, see text. The horizontal dotted lines indicate merger-to-galaxy mass ratios of 1:1, 1:4, and 1:10. The simulated galaxies have very complex star formation histories with large short-term variability that is often not directly related to galaxy mergers. Star forming galaxies tend to evolve along the star forming sequence but with frequent deviations by a factor of a few upwards (star bursts) and by orders of magnitude downwards (short-term suppression of star formation). Quiescent galaxies also show large variability but the average SFRs tend to fall below the level expected from the star forming sequence.

zeroth order, the sSFRs of galaxies evolves similar to the specific halo accretion rates (sHAR) of the parent dark matter haloes hosting these galaxies (e.g., Dekel et al. 2009; Yang et al. 2013; Lilly et al. 2013; Rodríguez-Puebla et al. 2016). However, in more detail there are significant differences.

For instance, the normalisation of the sSFR evolves faster at  $z < 1$  and slower at  $z > 1$  compared with the sHAR (e.g., Wein-

mann et al. 2011). Furthermore, the sSFR is typically larger than the sHAR by a factor of 2 (even after accounting for gas recycling from stellar mass loss) and also shows a mildly different residual trend with mass (Lilly et al. 2013). Stellar feedback and subsequent recycling likely play a crucial role in offsetting the evolution of the sSFR of galaxies from the zeroth order expectation set by the halo growth. The stellar mass – sSFR relation (and its evolution



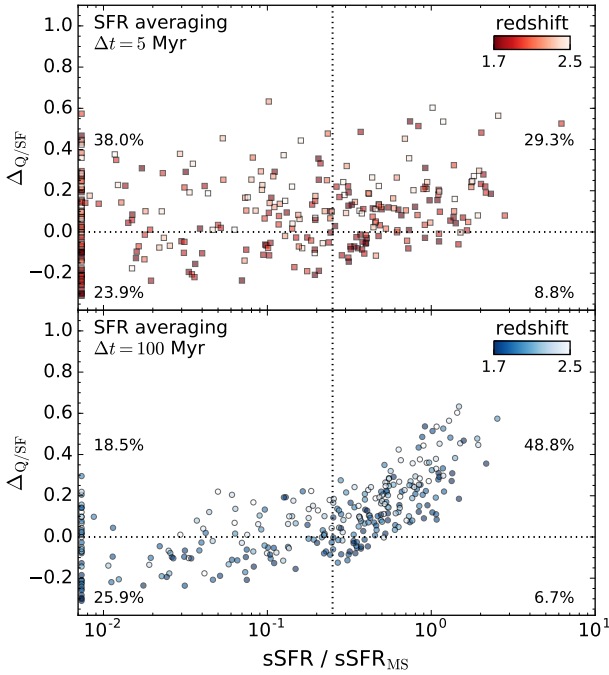


**Figure 8.** Distance from the boundary separating star forming and quiescent galaxies in colour space,  $\Delta_{Q/SF}$ , versus the offset from the star forming sequence. SFRs are measured over the past 5 Myr (top panel) or past 100 Myr (bottom panel). Only galaxies with  $M_{\text{star}} > 10^9 M_{\odot}$  at  $z = 1.7 - 2.5$  are included. Galaxies with sSFRs of a factor of 140 or more below the star forming sequence are shown at the left boundary in each panel. The dotted lines divide the space into 4 quadrants. The horizontal line separates quiescent from star forming galaxies based on colours, while the vertical line indicates a sSFR that is a factor 4 below the star forming sequence. Percentage values indicate the fraction of galaxies in each of the four quadrants. A colour-based classification into star forming and quiescent galaxies corresponds well to a classification based on sSFRs measured on  $\sim 100$  Myr timescales (bottom panel). In contrast, near-instantaneous sSFRs vary on short timescales and are thus poor predictors of galaxy colours (top panel).

with redshift) thus places important constraints on galaxy formation simulations.

Fig. 10 shows the relation between stellar mass and sSFR, the so-called ‘main sequence’ of star formation, for the galaxies in our sample at redshifts  $z = 4, 3, 2$ , and  $1.7$ . Clearly, galaxies at those redshifts show a large range in SFRs (here averaged over 100 Myr). However, much of this variation arises from the subset of quiescent galaxies and from galaxies with  $M_{\text{star}} < 10^{10} M_{\odot}$  at  $z \gtrsim 3$ . Massive galaxies that are star forming at  $z = 1.7 - 2$  have a rather narrow spread of SFRs at a given stellar mass, i.e., they form a star forming sequence with a typical sSFR of  $\sim 1 - 2 \text{ Gyr}^{-1}$ . Quiescent galaxies have a large range of (lower) sSFRs  $\sim 0.001 - 0.5 \text{ Gyr}^{-1}$ .

We perform a linear regression to the stellar mass – sSFR relation of all star forming, central galaxies at  $z = 1.7$  and  $z = 2$  that we simulated at HR resolution. Effectively, given the stellar mass selection of our sample, this limits the probed stellar mass range to  $\sim 10^{10} - 10^{11} M_{\odot}$ . The dispersion of the sSFR at given  $M_{\text{star}}$  is  $0.35^{+0.08}_{-0.04}$  dex. The confidence interval ( $1\sigma$ ) is obtained from bootstrapping. The logarithmic slope of the stellar mass – sSFR relation is consistent with zero within the  $1-\sigma$  confidence interval. The normalisation is  $\log_{10} \text{sSFR}[\text{yr}^{-1}] = -9.16^{+0.07}_{-0.11}$  for  $\log_{10} M_{\text{star}}[M_{\odot}] = 10.5$ . Our estimates are in similar to the measurement of the stellar mass – sSFR relation based on deep HST

and Herschel photometry (Schreiber et al. 2015), although perhaps with a  $\sim 0.2$  dex offset towards lower sSFRs. For  $z = 1.7 - 2$  galaxies, these authors report a dispersion of  $\sim 0.3$  dex, a vanishing slope, and a normalisation of  $\sim 10^{-9} \text{ yr}^{-1}$ . Similar values for the scatter were reported in other works (e.g., Rodighiero et al. 2010; Whitaker et al. 2012; Speagle et al. 2014; Salmon et al. 2015; Shivaee et al. 2015).

Reproducing the stellar mass – sSFR relation has long been a challenge for numerical simulations and semi-analytical models (e.g., Daddi et al. 2007; Furlong et al. 2015; Somerville & Davé 2015; Sparre et al. 2015; Johnston et al. 2015; Tomczak et al. 2016). In particular, simulations calibrated to reproduce  $z = 0$  observations often struggle to match the normalisation of the stellar mass – sSFR relation at  $z \sim 1 - 2$ . At such intermediate redshifts, the observed sSFRs of galaxies deviate noticeably from their specific halo accretion rates (e.g. Davé 2008; Sparre et al. 2015) and hydrodynamical simulations typically underpredict the sSFR by up to 0.5 dex (Sparre et al. 2015). The simulations presented in this paper fair somewhat better in matching the normalisation, slope, and scatter of the observed stellar mass – sSFR relation at  $z \sim 1.7 - 2$ . In addition, Hopkins et al. (2014) demonstrate that FIRE simulations with smaller halo masses ( $\sim 10^9 - 10^{12} M_{\odot}$  at  $z = 0$ ) reproduce the relation at redshifts  $z = 0 - 2$  as well.

Sparre et al. (2015) suggest that the difference between the simulated and the observed stellar mass – sSFR relation could be reduced if star formation histories were very bursty. Indeed, the FIRE approach of modelling stellar feedback predicts strongly fluctuating SFRs (Hopkins et al. 2014; Sparre et al. 2016; Muratov et al. 2015, and §3.1). Also, as shown explicitly in Hopkins et al. (2014), strong outflows driven by stellar feedback at high  $z$  lower the SFR at early times and increase the SFRs at subsequent times when the expelled gas falls back (see also Davé et al. 2011; Narayanan et al. 2015; Wang et al. 2015; Anglés-Alcázar et al. in prep). We thus speculate that efficient stellar feedback is responsible for bringing the predictions of MASSIVEFIRE into better agreement with observations at  $z \sim 1.7 - 2$ .

We can calculate the dispersion of the stellar mass – sSFR relation for the higher redshift (and lower mass) progenitors of  $z \sim 2$  galaxies. For the sub-sample of galaxies that are classified as star forming at their final snapshot ( $z \sim 1.7$  or  $z = 2$ ), we find that the scatter at  $z = 3$  is very similar ( $0.29^{+0.09}_{-0.03}$ ). However, the scatter increases at higher  $z$ , e.g., it is  $0.59^{+0.20}_{-0.10}$  at  $z = 4$ , not surprising given that the progenitors are, at those early times, small dwarfs with bursty star formation Sparre et al. (2016). We showed in §3.1 that almost all MASSIVEFIRE galaxies classified as quiescent at  $z \sim 1.7$  are identified as star forming at  $z \geq 3$ . Interestingly, the dispersion of the stellar mass – sSFR relation for these galaxies is generally high and does not strongly evolve with redshift ( $0.70^{+0.20}_{-0.09}$  at  $z = 1.7 - 2$ ,  $0.84^{+0.38}_{-0.18}$  at  $z = 3$ , and  $0.72^{+0.21}_{-0.04}$  at  $z = 4$ ). Apparently, galaxies at  $z = 3$  already “know” about their fate one Gyr later.

In Fig 11 we investigate this ‘memory’ effect in more detail using all galaxies in our sample that reside in moderately massive haloes ( $M_{\text{halo}} > 10^{12} M_{\odot}$ ). Specifically, we divide our sample into various subsamples and compare the evolution of the sSFRs, stellar masses, and halo masses of both the full sample and each of the subsamples. The first subsamples are created by dividing galaxies into star forming and quiescent based on their rest-frame UVJ colours at the final simulation snapshot ( $z = 1.7 - 2$ ). In addition, we compare galaxies that reside in slowly growing haloes at  $z \sim 2$  with those residing in quickly growing haloes. A specific growth rate (of the DM mass of the halo) of  $0.3 \text{ Gyr}^{-1}$  at  $z = 1.9$

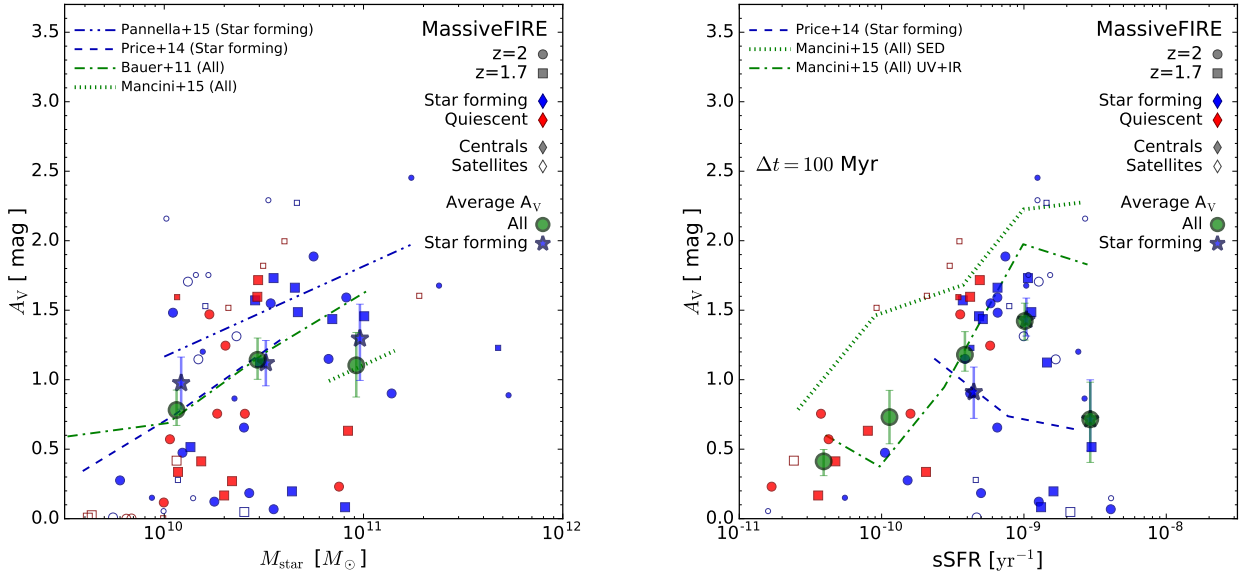


**Figure 9.**  $A_V$  vs. stellar mass (left) and specific SFR averaged over 100 Myr (right). Symbols are the same as in Fig. 6, except for the large circles (stars) that show the mean  $A_V$  in bins of  $M_{\text{star}}$  and  $s\text{SFR}$  for all galaxies (for star forming galaxies) in our sample. Lines show measurements of the dust extinction at  $z \sim 1.5 - 2$  (Bauer et al. 2011; Price et al. 2014; Mancini et al. 2015; Pannella et al. 2015). The amount of dust extinction increases with stellar mass and  $s\text{SFR}$ , perhaps saturating or reaching a maximum for galaxies near the star forming sequence ( $s\text{SFR} \sim 10^{-9} \text{ yr}^{-1}$  at  $z \sim 2$ ). Overall, our simulations predict levels of dust extinction in broad agreement with observations.

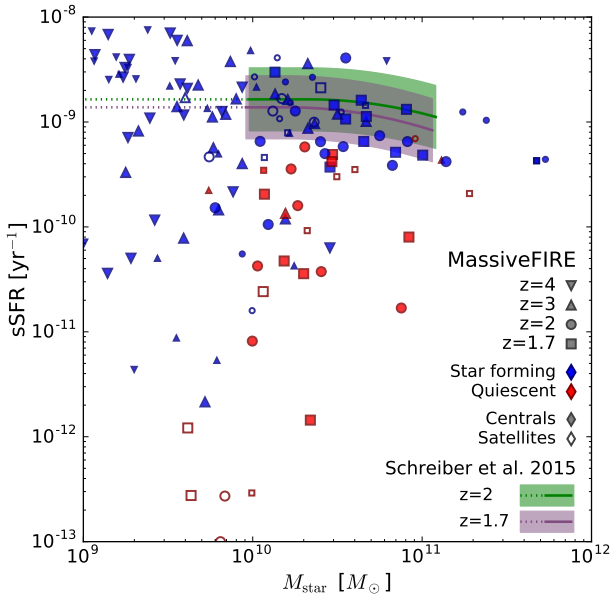


**Figure 10.** Specific star formation rate ( $s\text{SFR}$ ) vs. stellar mass. We split galaxies into quiescent and star forming (red vs. blue symbols) as well as centrals and satellites (filled vs. empty symbols). The different symbol shapes denote redshifts 4, 3, 2, and 1.7, see legend. Large and small symbols show HR runs (series A, B, and C) and MR runs (series Cm), respectively. The shaded areas show the observed stellar mass –  $s\text{SFR}$  relation at  $z = 1.7 - 2$  with a 0.3 dex scatter (Schreiber et al. 2015). Corrections to account for IMF differences are made. Dotted lines extrapolate these measurements to lower stellar masses. Massive galaxies identified as quiescent (star forming) according to their U–V and V–J colours generally lie below (fall onto) the observed star forming sequence.

is chosen as the dividing line (Feldmann et al. 2016). Third, we distinguish galaxies that grow their baryonic component (the sum of stellar mass and  $\text{H}_1 + \text{H}_2$  mass within  $0.1 R_{\text{halo}}$ ) at a specific rate below or above  $0.3 \text{ Gyr}^{-1}$  at  $z = 1.9$ . Furthermore, we compute the hot gas fraction  $f_{\text{hot gas}} = M_{\text{hot gas}} / (f_{\text{bar}} M_{180\text{m}})$ , where  $M_{\text{hot gas}}$  is the mass of halo gas with a temperature above  $2.5 \times 10^5 \text{ K}$  and  $f_{\text{bar}} = 0.163$  is the universal baryon fraction. We then divide galaxies depending on whether the hot gas fractions of their haloes are above or below a certain threshold. The median hot gas fraction of our sample is 0.35 and we adopted this value as our default threshold but discuss other choices as well.

Starting with the star forming and quiescent galaxy subsamples, Fig. 11 shows that the average  $s\text{SFR}$ s of the galaxies in the two sub-samples differ by a factor  $\sim 4 - 7$  at  $z \sim 2$  while the average stellar and halo masses are relatively similar. In addition, even at  $z \sim 4$ , the progenitors of  $z = 2$  quiescent galaxies have average  $s\text{SFR}$ s that are lower than those of the progenitors of star forming galaxies. This demonstrates that  $s\text{SFR}$ s at  $z > 2$  are not entirely driven by short-term physics but that they are also tied to the growth rate of their parent haloes.

Furthermore, the haloes harbouring  $z \sim 2$  quiescent galaxies tend to grow more slowly than the haloes of star forming galaxies at late times, in agreement with an earlier analysis of MASSIVEFIRE simulated galaxies (Feldmann et al. 2016). Also, quiescent galaxies assemble much of their stellar mass earlier than star forming galaxies of the same final stellar mass. Systematic differences in the stellar growth history of star forming and quiescent galaxies of same mass may have important practical implications for the accuracy of abundance matching techniques, as discussed in Clauwens et al. (2016).

Dividing galaxies based on the growth rates of their haloes leads to a very similar overall picture. In short, galaxies that reside

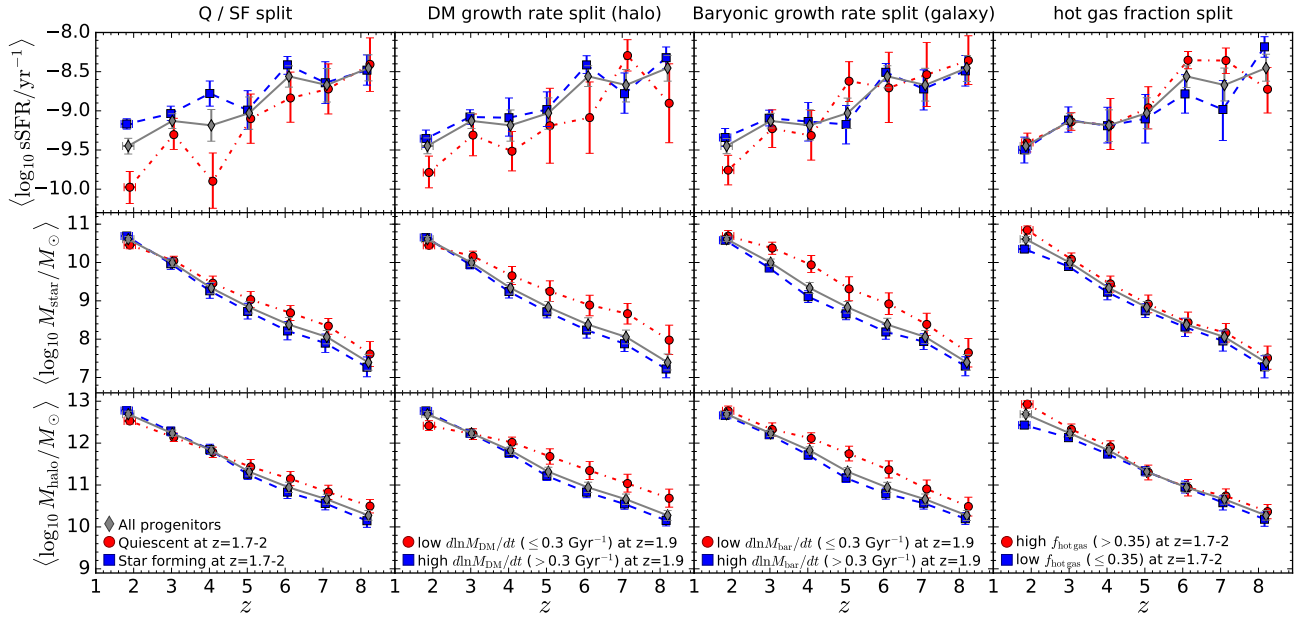


**Figure 11.** *Specific SFR, stellar masses, and halo masses of massive galaxies at  $z \sim 2$  and their progenitors.* We show average properties for galaxies with  $M_{\text{halo}}(z = 2) > 10^{12} M_{\odot}$  in our sample, split by their  $z = 1.7 - 2$  ‘quiescent’ status (1st column), growth rates of the DM mass of their haloes (2nd column), growth rate of their baryonic mass (3rd column), or their hot gas fractions within  $R_{\text{halo}}$  (4th column), see text for details. Rows show the evolution of the average sSFRs (top row), stellar masses (middle row), and halo masses (bottom row) of the selected galaxies and their main progenitors. The circular and square symbols are shifted by  $\Delta z = \pm 0.04$  for visualisation purposes. Error bars are computed via bootstrapping. The progenitor galaxies of  $z \sim 2$  galaxies that are quiescent or that have low halo / baryonic growth rates are typically more massive at higher redshift, reside in more massive haloes, and have lower sSFR than the progenitor galaxies of  $z \sim 2$  galaxies that are star forming or that have high halo / baryonic growth rates.

in slowly growing haloes at  $z \sim 2$  tend to have lower sSFRs than galaxies residing in quickly growing haloes. This is consistent with the picture of ‘cosmological starvation’, i.e., a link between the star formation rates of galaxies and the growth rates of their haloes. We stress that the halo growth rate is computed using only the dark matter mass of the halo, i.e., the growth rate should primarily be determined by the gravitational growth of cosmological structure. Consequently, it is plausible that a low halo growth rate *causes* a reduced star formation activity of galaxies instead of merely being correlated with it.

A qualitatively similar picture is obtained again if galaxies are divided based on the growth of their baryonic component. Galaxies that grow quickly tend to have higher sSFRs than galaxies that grow slowly. Furthermore, the stellar and halo mass growth histories differ. Unsurprisingly, galaxies that grow quickly (slowly) at late times tend to be less (more) massive and reside in less (more) massive haloes earlier on.

An interesting question is whether the reduced star formation activity in galaxies with low halo growth rates is related to the build-up of a hot gas halo. We therefore also split our sample into galaxies residing in haloes with high ( $> 0.35$ ) and low ( $\leq 0.35$ ) hot gas fractions of their haloes. We do not find a significant difference in their average sSFRs. This results also holds if we reduce the value of the critical hot gas fraction to 0.28 (the first quartile of the distribution of hot gas fractions) or increase it to 0.45 (the third quartile). However, galaxies with a higher hot gas fraction tend to be more massive and reside in more massive halo across the whole redshift range. Finally, we also increase the minimum temperature defining gas as ‘hot’ from  $2.5 \times 10^5$  K to  $10^6$  K. Again we find that galaxies with high and low hot gas fractions have comparable sSFRs. However, the higher temperature threshold increases the average stellar and halo masses of galaxies with high hot gas fractions

compared to those with low hot gas fractions. We conclude that the fraction of hot gas in moderately massive haloes of  $z \gtrsim 2$  galaxies is not a strong predictor of star formation activity. This conclusion could change once feedback from AGN is included.

### 3.4 Gas fractions and depletion times

Nearby star forming and quiescent galaxies differ not only in their colours, SFRs, and dust abundances, but also in their gas fractions. Specifically, at fixed stellar mass, quiescent galaxies harbour less neutral and molecular interstellar gas (e.g., Schiminovich et al. 2010; Saintonge et al. 2011; Serra et al. 2012). A qualitatively similar result appears to hold at high redshift although perhaps with a change in the overall normalisation (e.g., Sargent et al. 2015; Gobat et al. 2017). Overall, star forming galaxies with SFRs above the star forming sequence tend to have higher gas fractions and lower gas depletion times than galaxies that lie below the star forming sequence (Saintonge et al. 2011; Tacconi et al. 2013; Genzel et al. 2015; Scoville et al. 2016; Schinnerer et al. 2016).

The gas fractions of the galaxies in our sample are shown in Fig. 12. The main results shown by the figure are in qualitative agreement with observations. Specifically, we find that star forming galaxies tend to have higher gas fractions and slightly shorter gas depletion times than quiescent galaxies. Furthermore, gas-to-stellar mass ratios ( $\mu_{\text{gas}}$ ) scale with sSFRs. The scaling is sub-linear, however, implying that galaxies with low sSFRs are not only gas poor but also comparably inefficient in converting the existing gas into stars.

For a quantitative analysis we perform a linear regression between  $\log_{10} \mu_{\text{gas}}$  and  $\log_{10} \text{sSFR}$  for all central galaxies in our  $z = 1.7 - 2$  sample with stellar masses above  $10^{10} M_{\odot}$  and with sSFR in the range  $10^{-9.9} - 10^{-7.9} \text{ yr}^{-1}$ , similar to the proper-



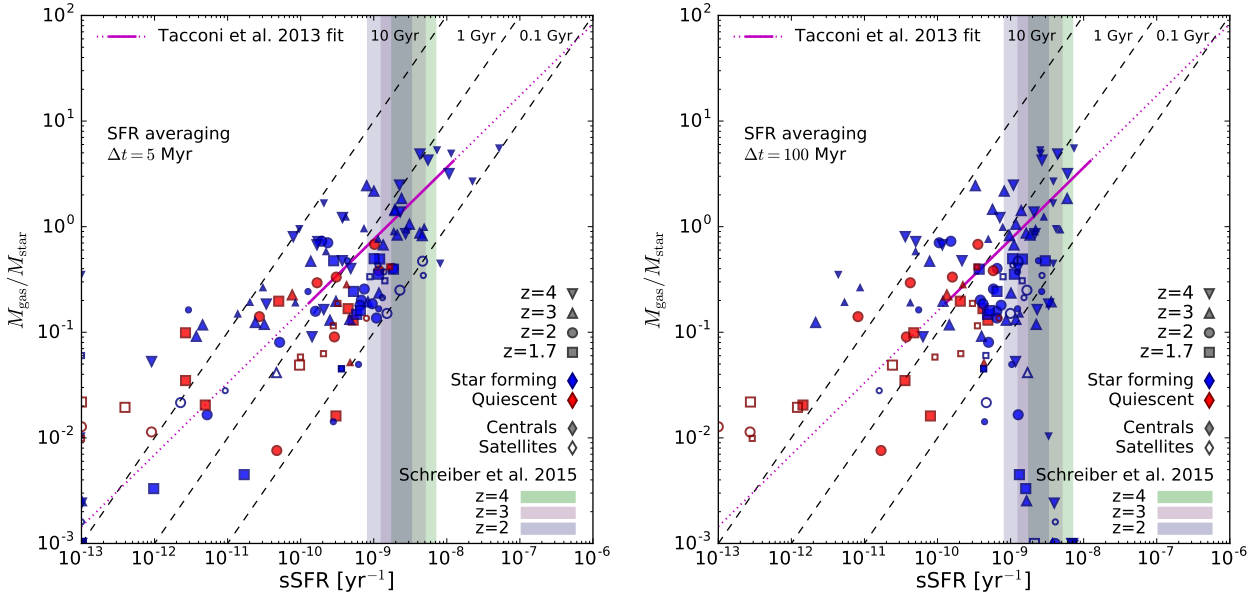


**Figure 12.** Gas fraction ( $M_{\text{gas}}/M_{\text{star}}$ ) versus  $s\text{SFR}$ . SFRs are measured on 5 Myr (left panel) and on 100 Myr (right panel) timescales. Diagonal dashed lines indicate depletion times ( $\text{SFR}/M_{\text{gas}}$ ) of 100 Myr, 1 Gyr, and 10 Gyr (from bottom to top). The vertical shaded regions indicate the position and spread of the star forming sequence reported by Schreiber et al. (2015) for  $M_{\text{star}} = 2 \times 10^{10} M_{\odot}$  galaxies. A fit to the observations by Tacconi et al. (2013) is shown by the solid magenta line. Extrapolations to lower and higher  $s\text{SFR}$ s are indicated by the dotted lines. Galaxies with  $s\text{SFR}$ s above the star forming sequence have both higher gas fractions and lower depletion times than galaxies on or below the star forming sequence. Quiescent galaxies tend to have lower gas fractions and longer depletion times than star forming galaxies.

ties of the sample of Tacconi et al. (2013). We find  $\log_{10} \mu_{\text{gas}} = 0.34(0.23) \log_{10}(\text{sSFR}/\text{Gyr}) - 0.55(0.09)$ . While the slope is consistent with Tacconi et al. (2013) given statistical errors, our simulations predict at face value lower gas fractions by  $\sim 0.4$  dex. However, gas fractions depend somewhat sensitively on the radius within they are measured. For instance, increasing the radius within which  $\mu_{\text{gas}}$  and  $s\text{SFR}$ s are measured from 5 to 10 kpc changes the regression result to  $\log_{10} \mu_{\text{gas}} = 0.51(0.18) \log_{10}(\text{sSFR}/\text{Gyr}) - 0.34(0.08)$ . The offset between simulation predictions and observations is now  $\sim 0.2$  dex. The combined systematic uncertainties of SFR, stellar mass, and especially gas mass estimates are likely significantly larger than 0.2 dex.

The relation between  $\mu_{\text{gas}}$  and  $s\text{SFR}$  is significantly tighter if near-instantaneous SFRs are used instead of SFRs averaged over long timescales. This is not surprising as the instantaneous SFRs in our simulations (as well as in nature) depends primarily on the presence of (dense molecular) gas. SFRs measured on 100 Myr correlate well with galaxy colours (see Fig. 8) but lag behind short-term changes in the gas reservoirs. Consequently, long SFR averaging timescales result in transition galaxies that are still ‘on’ the star forming sequence but have low gas fractions (galaxies leaving the star forming sequence) as well as gas-rich galaxies with low  $s\text{SFR}$ s (galaxies returning to the star forming sequence). Galaxies classified as quiescent based on their colours are much less sensitive to the choice of the SFR averaging timescale than star forming galaxies. This finding is consistent with the result presented in §3.1 that quiescent galaxies experience prolonged periods of reduced star formation activity while the SFRs of many star forming galaxies fluctuate strongly on short timescales.

### 3.5 The environments of quiescent and star forming galaxies

A large body of observational evidence points to a link between the environment of galaxies and their star formation activity (e.g., Dressler et al. 1985; Baldry et al. 2006; Weinmann et al. 2010; Peng et al. 2010; McGee et al. 2011). At  $z \leq 1$  the likelihood that a galaxy is ‘quenched’, i.e., that its SFR is much lower than those of star forming galaxies of similar stellar masses, increases both with the stellar mass and the environmental overdensity (Peng et al. 2010). Kovac et al. (2014) argue that the environmental dependence has its origin in a higher satellite quenching efficiency in denser environments. Hence, ‘environmental quenching’ is perhaps a result of environmental processes that affect primarily member galaxies of groups and clusters via, e.g., ram pressure stripping, tidal stripping, or harassment. However, environmental processes may leave an imprint out to 2-3 virial radii Balogh et al. (2000) and, hence, may also affect a large fraction of central galaxies (Cen 2014).

Feldmann & Mayer (2015) and Feldmann et al. (2016) argue that a significant fraction of massive galaxies at  $z \sim 2$  are subject to an additional process related to the gravity-driven growth of dark matter haloes. In particular, they show that quiescent (star forming) galaxies at  $z \sim 2$  reside preferentially in haloes with low (high) dark matter accretion rates. This process, ‘cosmological starvation’, does not explain why the quiescent fraction strongly increases with stellar mass at  $z \lesssim 1$  but it sheds light on the co-existence of  $z \sim 2$  star forming and quiescent central galaxies with the same stellar mass.

In this section we discuss the environments of quiescent and star forming galaxies in our sample. This analysis complements the work by Feldmann et al. (2016) who discuss the fractions of star forming and quiescent galaxies in MASSIVEFIRE and their dependences on stellar mass.

We study this using two different measures of the local environment (§2.4). The local environmental density,  $\rho$ , includes all

matter within a sphere of  $5 R_{\text{halo}}$  centred on a given halo but with the halo itself excluded, while the Hill radius,  $R_{\text{Hill}}$ , defines a minimal distance beyond which material is no longer gravitationally bound to the primary halo. The latter is also related to the maximal tidal force exerted by neighbouring haloes on the primary halo (Hahn et al. 2009).

We plot the local environmental density of our galaxies as function of the Hill radii of their haloes in Fig. 13. Both measures of environments are clearly correlated. Galaxies residing in regions with a larger environmental density have shorter Hill radii. This result is expected, as the presence of neighbouring massive haloes increases both the environmental density and decreases the Hill radius (Hearin et al. 2016). For satellites,  $R_{\text{Hill}}$  ( $\rho$ ) is dominated by the parent halo, hence they have the smallest (largest) values of  $R_{\text{Hill}}$  ( $\rho$ ). The locus of the density – Hill radius relation does not evolve strongly with redshift over the  $z = 1.7 - 3$  range.

Fig. 13 shows that star forming centrals span the whole range of Hill radii while quiescent centrals are clustered at  $R_{\text{Hill}} \sim 1 - 2$  and  $R_{\text{Hill}} \sim 7 - 11$ . This bimodal distribution is statistically significant (according to a dip test, Hartigan & Hartigan 1985) even given our small sample size.

Quiescent centrals with large  $R_{\text{Hill}}$  are more massive ( $M_{\text{star}} \sim 2 - 9 \times 10^{10}$ ) than those with small  $R_{\text{Hill}}$  ( $M_{\text{star}} \sim 1 - 2 \times 10^{10}$ ) adding further evidence that they belong to two different classes of galaxies. All quiescent galaxies with large  $R_{\text{Hill}}$  reside at the centres of specifically targeted (‘primary’) MASSIVE-FIRE haloes, see §2.1. In contrast, most of the quiescent centrals with low  $R_{\text{Hill}}$  reside in isolated haloes that happen to lie in one of the highly-resolved zoom-in regions.

Quiescent centrals with small  $R_{\text{Hill}}$  values are likely tidally affected by the presence of nearby massive haloes (Wang et al. 2007) and, hence, need to compete with those haloes for the gas in their vicinity. We thus confirm that environmental effects can alter the SFRs and colours of galaxies at several kpc from massive haloes. The low  $R_{\text{Hill}}$  quiescent galaxies appear to form a continuous sequence matching quiescent satellites. The physics driven the SFR and colour evolution might be the same in both cases, low  $R_{\text{Hill}}$  quiescent galaxies just have not yet crossed the halo to become satellites.

### 3.6 Stellar mass – Halo mass relation

Stellar masses of galaxies do not scale linearly with the masses of their parent dark matter haloes (e.g., More et al. 2011; Yang et al. 2012; Moster et al. 2013; Behroozi et al. 2013; Shankar et al. 2014; van Uitert et al. 2016). Cosmological simulations of galaxies have been struggling to reproduce this observation quantitatively (e.g., Scannapieco et al. 2012; Martizzi et al. 2012), although significant advances have been made in recent years in the modelling galaxies of low to moderate masses (e.g., Guedes et al. 2011; Aumer et al. 2013; Munshi et al. 2013; Hopkins et al. 2014). Much of the recent progress stems from the realisation by many research groups that stellar feedback has to be modelled more accurately in order to retain its effectiveness in regulating star formation and in generating galactic outflows. Some challenges remain, however, as it is unclear, for instance, whether stellar feedback is sufficient to reduce the gas-to-star conversion efficiency in massive galaxies to the observed level. Simulations without AGN feedback typically predict stellar masses of massive galaxies that are at least a factor 2 too high (e.g., Feldmann et al. 2010; Martizzi et al. 2012). However, in contrast with the stellar feedback model adopted here, see §2.2,

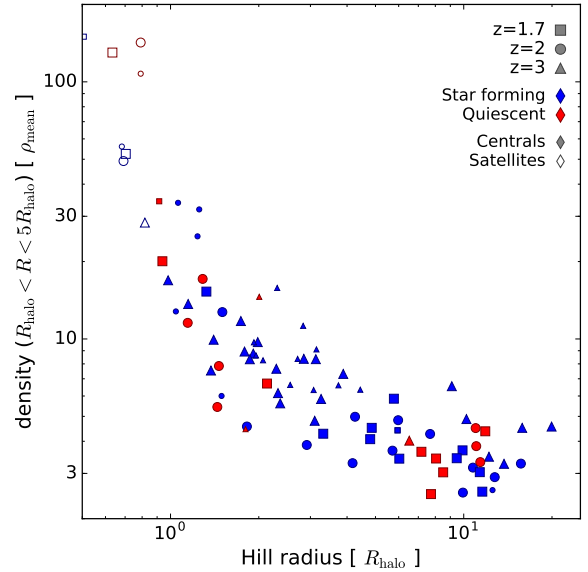


**Figure 13.** Local environmental density as function of Hill radius. The y-axis shows the matter density within a shell  $R_{\text{halo}} < R < 5 R_{\text{halo}}$  in units of the mean density of the Universe at the given epoch. The x-axis shows the Hill radius (see text) associated with each galaxy in units of its  $R_{\text{halo}}$ . In contrast with star forming galaxies, quiescent centrals in our sample have a bimodal distribution of Hill radii clustered around  $\sim R_{\text{halo}}$  and  $\sim 10 R_{\text{halo}}$ .

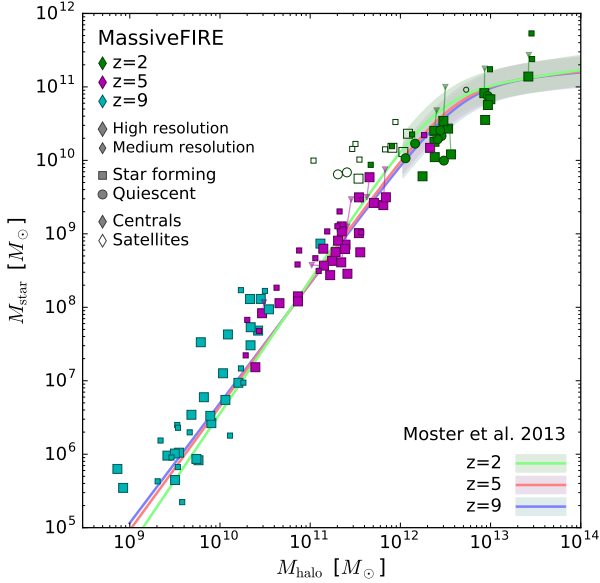
many of the previous models do not account for the full energy and momentum input from stellar sources.

Fig. 14 shows that the relation between  $M_{\text{star}}$  and  $M_{\text{halo}}$  for our sample is in good agreement with the empirically derived relation based on abundance matching (Moster et al. 2013). The agreement holds over five orders of magnitude in halo mass and over a large redshift range<sup>5</sup>. The predicted stellar masses at  $z \sim 2$  are somewhat on the lower side. There are several possible explanations, such as stellar feedback being too efficient in our simulations or our simulations underestimating cooling from the halo, perhaps due to uncertainties in how gas mixing is handled.

Table B2 in the Appendix provides more detail on the SHMR of central galaxies in the MASSIVEFIRE sample for different halo mass and redshift ranges. The logarithmic slope changes from about two for  $10^9 - 10^{11} M_{\odot}$  haloes at  $z = 9$ , to less than one for  $10^{12} - 10^{14} M_{\odot}$  haloes at  $z = 1.7 - 2$ . We do not find strong evidence that the SHMR is significantly different for star forming and quiescent galaxies at  $z = 2$ . We note that the limited size of our sample prevents us from detecting small differences with statistical significance.

We calculate the scatter of the relation between  $\log_{10} M_{\text{star}}$  and  $\log_{10} M_{\text{halo}}$  via a least squares linear regression, excluding satellite galaxies. The scatter is about 0.2 dex for our sample at

<sup>5</sup> The Moster et al. 2013 predictions are derived based on stellar mass functions that span the  $z = 0 - 4$  range and for halo masses  $> 10^{11} M_{\odot}$ , i.e., the  $z = 9$  curve is an extrapolation. Our predicted SHMR is also in agreement with the fit from Behroozi et al. 2013 that incorporates stellar mass function estimates at higher  $z$ . It should be noted that abundance-matching estimates at high redshift suffer from significant systematic uncertainties.



**Figure 14.** Stellar mass – halo mass relation (SHMR) of the galaxies in our sample. The plot shows stellar and halo masses at  $z = 2$  (green symbols, top right),  $z = 5$  (purple, middle), and  $z = 9$  (cyan, bottom left). Circles and squares indicate whether galaxies are classified as quiescent and star forming, respectively, according to the UVJ criterion (Whitaker et al. 2011). Filled and empty symbols distinguish central from satellite galaxies. Large (small) symbols show simulations run at high (medium) resolution. Small triangles show MR re-simulations of HR runs (solid lines connect the corresponding runs). The three dotted lines show the abundance matching estimate (Moster et al. 2013) of the SHMR and its extrapolation to high redshifts and low stellar masses. Halo masses by Moster et al. (2013) are converted to match the definition of §2.1 using an average halo mass – concentration relation, see Kravtsov et al. (2014). The overlapping semi-transparent patches show the expected scatter of 0.2 dex from the mean relation in  $M_{\text{halo}} \gtrsim 10^{12} M_{\odot}$  haloes (Moster et al. 2013; Behroozi et al. 2013; Reddick et al. 2013). The simulations agree well with predictions from abundance matching for haloes in the  $M_{\text{halo}} \sim 10^{10} - 10^{13} M_{\odot}$  range.

$z \sim 2$ . This amount of scatter agrees with estimates based on abundance matching constraints, kinematic measurements, and weak lensing maps for galaxies in  $\gtrsim 10^{12} M_{\odot}$  haloes at lower redshifts (e.g., More et al. 2009; Leauthaud et al. 2012; Behroozi et al. 2013; Reddick et al. 2013). The scatter is larger for the less massive progenitor galaxies at higher  $z$  (e.g.,  $\sim 0.25$  dex at  $z \sim 7$ ) but at  $z = 0$  such low mass haloes also exhibit larger scatter (the precise value is currently not well constrained, e.g., Brook et al. 2015; Garrison-Kimmel et al. 2016.)

The parent haloes of galaxies in our sample span a broad range of halo masses, up to  $10^{13.5} M_{\odot}$ . If we assume that the SHMR is not strongly evolving with redshift at  $z \geq 2$ , e.g., Moster et al. (2013), but cf. Behroozi et al. (2013), then we can combine our data from different redshift epochs ( $z \sim 1.7 - 9$ ) and fit the SHMR over the large mass range sampled by MASSIVEFIRE. A quadratic dependence

$$\log_{10}(M_{\text{star}}/M_{\text{halo}}) = -0.089^{+0.019}_{-0.015} [\log_{10}(M_{\text{halo}}/M_{\odot}) - 12.91^{+0.41}_{-0.23}]^2 - 2.20^{+0.05}_{-0.03}$$

is visually a good fit to the MASSIVEFIRE data (reduced  $\chi^2$  of

1.39 if we assume a fixed dispersion of 0.25 dex). The ratio between stellar mass of the galaxy and halo mass reaches a maximum for haloes with  $M_{\text{halo}} \sim 10^{12.9} M_{\odot}$ , perhaps slightly higher than, but still in approximate agreement with, estimates based on abundance matching at  $z \sim 2$ . We can also fit  $M_{\text{star}}/M_{\text{halo}}$  with the double power law suggested by Moster et al. (2013) that has 4 free parameters (their equation 2). The fitted slope in the low mass regime,  $\beta = 0.63^{+0.18}_{-0.11}$ , is consistent with the  $\beta$  value reported by Moster et al. (2013) for redshift 2.

#### 4 SUMMARY AND CONCLUSIONS

This paper analyses the global properties of over 30 massive galaxies at  $z \sim 2$  that were simulated in high-resolution, cosmological zoom-in simulations (MASSIVEFIRE). We focus in particular on the differences between star forming and quiescent galaxies residing in or near group-sized haloes ( $M_{\text{halo}} \sim 10^{12.5} - 10^{13.5} M_{\odot}$ ) at  $z \sim 2$ . The resolution, numerical methods, and the modelling of star formation and stellar feedback match previous runs by the FIRE project (Hopkins et al. 2014; Faucher-Giguere et al. 2015) but here we study galaxies residing in order-of-magnitude more massive haloes. The modelling approach adopted by FIRE has been validated against observations in a number of published works (see introduction) allowing us to explore the evolution of massive galaxies in the absence of AGN feedback.

In this paper, we focus on the colours, masses, SFRs, and environments of star forming and quiescent galaxies. Additional properties, such as galaxy sizes and ISM properties, will be discussed in future work. Our simulations include galaxies with a range of morphologies, including dusty disk galaxies, star forming irregular galaxies, and early type galaxies with low dust content and reduced SFRs. About 1/3 of the galaxies in the sample have an extended ( $> \text{kpc}$ ) stellar disk, see Figs. 2 and 3.

Galaxies are divided into star forming or quiescent based on rest-frame U, V, and J colours. Furthermore, galaxies are classified as centrals or satellites depending on whether they reside at the centres of isolated haloes or sub-haloes, respectively. Quiescent galaxies make up about half the sample at  $z \sim 2$  and are comprised in about equal parts of centrals and satellites. The quiescent fraction of our sample decreases with increasing redshift reaching zero at  $z = 4$ . However, because we follow the evolution of a specific set of galaxies, their  $z \sim 4$  progenitors are not massive galaxies (none with  $M_{\text{star}} \gtrsim 10^{10} M_{\odot}$ ). Two-thirds of the star forming galaxies at  $z \sim 2$  in our sample are centrals and one-third are satellites.

Various properties of observed galaxies are reproduced reasonably well in these simulations despite the absence of AGN feedback. Simulated galaxies show a similar mix of morphologies (e.g., star forming disk galaxies, irregular galaxies, dust-poor early type galaxies; Fig. 2), a reasonable scaling of dust extinction with stellar mass and SFR (Fig. 9), and both a stellar mass – sSFR relation (Fig. 10) and a stellar mass – halo mass relation (Fig. 14) with normalisation and scatter in broad agreement with observations. Gas fractions in the simulations are in rough agreement with observations although perhaps somewhat biased low (Fig. 12). On the other hand, the simulations do not account for the observed population of massive galaxies with the reddest U-V colours (Fig. 4). Furthermore, they do not show clear evidence for a colour bimodality at  $z \sim 2$ .

Our main findings include the following:

- (i) Galaxies migrate between the star forming and quiescent populations as the colours of their stellar populations change and



evolve. Our sample includes both galaxies that are quiescent for only a brief period of time ( $< 100$  Myr) as well as those that become quiescent and remain so for up to 1 Gyr, in roughly comparable numbers. The classification of galaxies into quiescent and star forming is not sensitive to the chosen line-of-sight.

(ii) The broad-band colours of our simulated galaxies reasonably overlap with those of observed galaxies at  $z \sim 2$ . However, there appear to be significant differences in detail. In particular, our simulations do not produce galaxies with very red U–V colours ( $U - V > 1.6$ ) and they also predict a significant fraction of star forming galaxies somewhat closer to the star forming vs. quiescent separation than observed.

(iii) We do not find statistically significant evidence for a colour bimodality in our sample. However, our simulation sample is likely too small to detect a colour bimodality even if present (see Appendix A).

(iv) Galaxies at  $z \sim 2$  that are classified as quiescent based on their U–V and V–J colours come in two varieties, see Fig. 9. The first class consists of galaxies with low sSFR and relatively low amounts of dust extinction ( $A_V \sim 0.3$  mag). The second class includes galaxies with somewhat reduced sSFR (compared to the star forming sequence) that harbour significant amounts of dust ( $A_V \sim 1.5$  mag). Light from on-going star formation in these galaxies is largely blocked by the dust and the stellar colours are dominated by older stars.

(v) The star forming galaxies in our sample reproduce the observed relation between stellar masses and sSFRs at  $z \sim 1.7 - 2$ , i.e., the star forming (‘main’) sequence, including normalisation ( $1-2 \text{ Gyr}^{-1}$ ) and scatter ( $\sim 0.3$  dex). The SFR histories of individual galaxies are bursty, with starbursts followed by a brief ( $\lesssim 100$  Myr) suppression of star formation activity, and subsequent return to the star forming sequence. In most cases, these starbursts are not triggered by galaxy mergers.

(vi) The SFRs of high redshift galaxies are affected by both internal processes (starbursts and outflows) that change the SFR on short ( $< 100$  Myr) timescales, see Fig. 7, as well as external processes (e.g., cosmological starvation) that determine the average SFRs and galaxy colours over longer time scales, see Fig. 11.

(vii) The median dust extinction of our sample increases with time as galaxies become more massive and metal-rich. The  $A_V$  distributions of star forming centrals and star forming satellites are statistically indistinguishable. At  $z \sim 1.7 - 2$ , the dust extinction is significantly higher in star forming galaxies than in quiescent galaxies.

(viii) The Hill radius of a halo is a good proxy for the local environmental density. Galaxies residing in denser (less dense) environments have smaller (larger) Hill radii. The Hill radius distribution of quiescent *centrals* is bimodal (Fig. 13), suggesting perhaps different pathways for reducing the star formation activity in central galaxies depending on environment.

(ix) The predicted stellar mass – halo mass relation (SHMR) agrees with the observed relation over 5 orders of magnitude in halo mass, see Fig. 14. This finding extends the result previously found for lower-mass galaxies simulated with FIRE physics (Hopkins et al. 2014). The scatter of the SHMR is  $\sim 0.2$  dex for massive galaxies at  $z \sim 2$ .

(x) The average stellar masses (and halo masses) of star forming and quiescent central galaxies in our sample at  $z \sim 2$  are comparable. However, the  $z \geq 4$  progenitors of  $z \sim 2$  star forming centrals are typically less massive than the progenitors of quiescent centrals. Hence, stellar and halo masses of star forming centrals grow faster between  $z \sim 2 - 4$  than those of quiescent centrals.

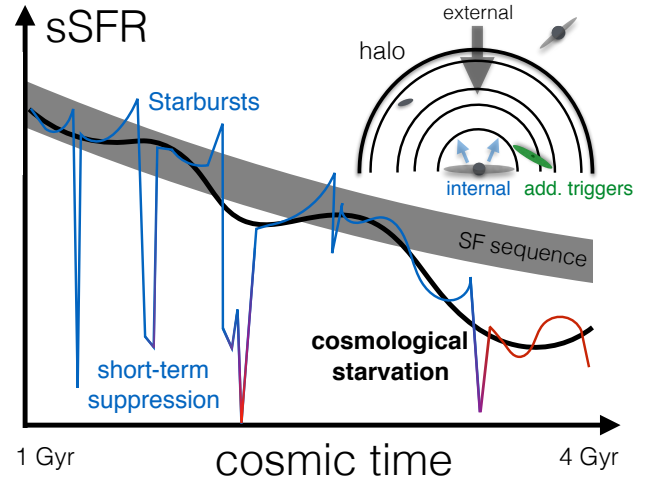


**Figure 15.** Schematic representation of the SFR evolution of simulated central galaxies with moderate masses at the Cosmic Noon (neglecting AGN feedback). At early times ( $z \gtrsim 3$ ), the sSFRs of central galaxies co-evolve with the star forming sequence. However, starbursts and outflows triggered by various internal and external processes can result in brief, but severe, interruptions. Processes external to galaxies, such as cosmological starvation, resulting from, e.g., entering a denser environment, being accreted as a satellite, or residing in a low density region, drive long-term changes to the star formation history and, hence, modulate galaxy colours.

Our findings suggest that, in our simulations, the SFRs and colours of moderately massive galaxies at  $z \sim 2$  and their higher redshift progenitors are affected by two separate processes, see Fig. 15. First, starbursts and outflows triggered by various internal and external mechanisms frequently lead to brief, but severe, deviations from the star forming sequence. These deviations occur less often at later times when galaxies are more massive and cosmological accretion and merger rates are declining. In many cases, expelled or consumed gas is replenished quickly at high redshift (e.g., Tacchella et al. 2016) and, hence, these “quenching” events tend to be short-lived. Secondly, absent additional mechanisms of removing gas from galaxies (see below), galaxies likely need to reduce the rate at which they *accrete gas* from their surroundings if their star formation activity is to decrease for extended periods of time ( $> 100$  Myr). Various pathways to reduce gas accretion onto galaxies have been studied in the literature (e.g., halo quenching, environmental processes) and they likely all play a role depending on the circumstances. Additional quenching processes are also likely necessary to explain the observed scaling of quiescent fraction with stellar mass at  $z \lesssim 1$ .

We clearly identify both traditional satellites and a significant population of formally ‘central’, quiescent galaxies within a few  $R_{\text{halo}}$  of more massive haloes, where environmental processes (e.g., ram pressure and tidal forces) likely reduce gas accretion and dominate the suppression of star formation. For the sub-population of our sample that are truly isolated centrals with more sustained ( $\gtrsim 100$  Myr) quiescent periods, we argue that their reduced growth at  $z \sim 2$  is a consequence of assembling a large fraction of their final halo and stellar mass at earlier times.

The stellar masses and star formation rates of our simulated galaxies at  $z \sim 2$  are in broad agreement with observations. We attribute this success largely to the detailed and accurate modelling of stellar feedback processes and to the high numerical resolution ( $\sim 10$  pc,  $\sim 10^{4.5} M_{\odot}$ ) of our simulations. However, our sample of

galaxies does not show a colour bimodality at  $z \sim 2$ . Furthermore, the U–V colours of our simulated galaxies are not as red as those of many observed quiescent galaxies at those redshifts.

The absence of a clear colour bimodality is likely related to the large number of galaxies with intermediate colours in our simulations. Stellar feedback driven outflows typically do not suppress star formation long enough to turn colours sufficiently red (Fig. 8), resulting in many galaxies with intermediate ("green") colours. Cosmological starvation helps to redden galaxy colours by reducing the overall level of star formation activity but may also move galaxies from the star forming sequence into the green valley.

AGN feedback (and/or other processes) may be important in resolving these differences. For example, the energy and momentum injection from AGNs could potentially fully suppress any residual star formation. AGN feedback may thus help to produce (and extend the duty cycle of) a larger number of galaxies with zero SFR at high  $z$  (Kriek et al. 2006) as well as redden galaxy colours further, creating a visible colour bimodality. In addition, AGN feedback is likely an effective mechanism to reduce the cooling rate of gas, and thus the SFR, in massive galaxies at late times (Croton et al. 2006). Finally, galactic outflows powered by AGN could affect the overall content, chemistry, and structure of the CGM. We plan to study the role and impact of AGN feedback for massive galaxies in future work.

## ACKNOWLEDGMENTS

RF thanks the referee for suggestions that helped to improve the quality of the paper. RF was supported in part by NASA through Hubble Fellowship grant HF2-51304.001-A awarded by the Space Telescope Science Institute, which is operated by the Association of Universities for Research in Astronomy, Inc., for NASA, under contract NAS 5-26555, in part by the Theoretical Astrophysics Center at UC Berkeley, and by NASA ATP grant 12-ATP-120183. RF also acknowledges financial support from the Swiss National Science Foundation (grant no 157591). EQ was supported by NASA ATP grant 12-ATP-120183, a Simons Investigator award from the Simons Foundation, and the David and Lucile Packard Foundation. Support for PFH was provided by an Alfred P. Sloan Research Fellowship, NASA ATP Grant NNX14AH35G, and NSF Collaborative Research Grant #1411920 and CAREER grant #1455342. CAFG was supported by NSF through grants AST-1412836 and AST-1517491, and by NASA through grant NNX15AB22G. DK was supported by NSF grant AST-1412153 and by a Cottrell Scholar Award. Simulations were run with resources provided by the NASA High-End Computing (HEC) Program through the NASA Advanced Supercomputing (NAS) Division at Ames Research Center, proposal SMD-14-5492. Additional computing support was provided by HEC allocations SMD-14-5189, SMD-15-5950, and NSF XSEDE allocations AST120025, AST150045. This work made extensive use of the NASA Astrophysics Data System and arXiv.org preprint server.

## REFERENCES

- Abadi M. G., Moore B., Bower R. G., 1999, *Mon. Not. R. Astron. Soc.*, 308, 947  
 Agertz O., et al., 2007, *Mon. Not. R. Astron. Soc.*, 380, 963  
 Agertz O., Kravtsov A. V., Leitner S. N., Gnedin N. Y., 2013, *Astrophys. J.*, 770, 25  
 Alexander D., Hickox R., 2012, *New Astron. Rev.*, 56, 93  
 Aravena M., et al., 2016, *Mon. Not. R. Astron. Soc.*, 457, 4406  
 Aumer M., White S. D. M., Naab T., Scannapieco C., 2013, *Mon. Not. R. Astron. Soc.*, 434, 3142  
 Bahe Y. M., McCarthy I. G., 2015, *Mon. Not. R. Astron. Soc.*, 447, 969  
 Bahe Y. M., McCarthy I. G., Balogh M. L., Font a. S., 2013, *Mon. Not. R. Astron. Soc.*, 430, 3017  
 Baldry I. K., Balogh M. L., Bower R., Glazebrook K., Nichol R. C., 2004, *Distribution*, p. 14  
 Baldry I. K., Balogh M. L., Bower R. G., Glazebrook K., Nichol R. C., Bamford S. P., Budavari T., 2006, *Mon. Not. R. Astron. Soc.*, 373, 469  
 Balogh M. L., Navarro J. F., Morris S. L., 2000, *Astrophys. J.*, 540, 113  
 Balogh M. L., Baldry I. K., Nichol R., Miller C., Bower R., Glazebrook K., 2004, *Astrophys. J.*, 615, L101  
 Bauer A. E., Conselice C. J., Pérez-González P. G., Grützbauch R., Bluck A. F. L., Buitrago F., Mortlock A., 2011, *Mon. Not. R. Astron. Soc.*, 417, 289  
 Behroozi P. S., Wechsler R. H., Conroy C., 2013, *Astrophys. J.*, 770, 57  
 Bezanson R., van Dokkum P. G., Tal T., Marchesini D., Kriek M., Franx M., Coppi P., 2009, *Astrophys. J.*, 697, 1290  
 Blanton M. R., et al., 2003, *Astrophys. J.*, 594, 186  
 Bouché N., et al., 2010, *Astrophys. J.*, 718, 1001  
 Bouwens R. J., et al., 2009, *Astrophys. J.*, 705, 936  
 Brammer G. B., et al., 2009, *Astrophys. J.*, 706, L173  
 Brammer G. B., et al., 2011, *Astrophys. J.*, 739, 24  
 Brinchmann J., Charlot S., White S. D. M., Tremonti C., Kauffmann G., Heckman T., Brinkmann J., 2004, *Mon. Not. R. Astron. Soc.*, 351, 1151  
 Brook C. B., Cintio A. D., Di Cintio A., 2015, *Mon. Not. R. Astron. Soc.*, 450, 3920  
 Bruzual G., Charlot S., 2003, *Mon. Not. R. Astron. Soc.*, 344, 1000  
 Calzetti D., Armus L., Bohlin R. C., Kinney A. L., Koornneef J., Storchi-Bergmann T., 2000, *Astrophys. J.*, 533, 682  
 Carollo C. M., et al., 2013, *Astrophys. J.*, 773, 112  
 Cattaneo a., Dekel A., Devriendt J., Guiderdoni B., Blaizot J., 2006, *Mon. Not. R. Astron. Soc.*, 370, 1651  
 Cen R., 2014, *Astrophys. J.*, 781, 38  
 Ceverino D., Dekel A., Tweed D., Primack J., 2015, *Mon. Not. R. Astron. Soc.*, 447, 3291  
 Chabrier G., 2003, *Publ. Astron. Soc. Pacific*, 115, 763  
 Chan T. K., Kereš D., Oñorbe J., Hopkins P. F., Muratov A. L., Faucher-Giguère C.-A., Quataert E., 2015, *Mon. Not. R. Astron. Soc.*, 454, 2981  
 Choi E., Naab T., Ostriker J. P., Johansson P. H., Moster B. P., 2014, *Mon. Not. R. Astron. Soc.*, 442, 440  
 Clauwens B., Franx M., Schaye J., 2016, *Mon. Not. R. Astron. Soc.*, 000, 1  
 Conselice C. J., 2014, *Annu. Rev. Astron. Astrophys.*, 52, 291  
 Croton D. J., et al., 2006, *Mon. Not. R. Astron. Soc.*, 365, 11  
 Cullen L., Dehnen W., 2010, *Mon. Not. R. Astron. Soc.*, 408, 669  
 Daddi E., et al., 2005, *Astrophys. J.*, 626, 680  
 Daddi E., et al., 2007, *Astrophys. J.*, 670, 156  
 Daddi E., et al., 2010, *Astrophys. J.*, 713, 686  
 Damjanov I., et al., 2011, *Astrophys. J.*, 739, L44  
 Davé R., 2008, *Mon. Not. R. Astron. Soc.*, 385, 147  
 Davé R., Oppenheimer B. D., Finlator K., 2011, *Mon. Not. R. Astron. Soc.*, 415, 11  
 Davé R., Finlator K., Oppenheimer B. D., 2012, *Mon. Not. R. Astron. Soc.*, 421, 98  
 Dehnen W., Aly H., 2012, *Mon. Not. R. Astron. Soc.*, 425, 1068  
 Dekel A., Birnboim Y., 2006, *Mon. Not. R. Astron. Soc.*, 368, 2  
 Dekel A., Birnboim Y., 2007, *Mon. Not. R. Astron. Soc.*, 383, 119  
 Dekel A., Burkert A., 2014, *Mon. Not. R. Astron. Soc.*, 438, 1870  
 Dekel a., et al., 2009, *Nature*, 457, 451  
 Di Matteo T., Springel V., Hernquist L., 2005, *Nature*, 433, 604  
 Dressler A., Thompson I. B., Sackett S. A., 1985, *Astrophys. J.*, 288, 481  
 Dunlop J. S., et al., 2016, arXiv  
 Fabian A., 2012, *Annu. Rev. Astron. Astrophys.*, 50, 455  
 Farouki R., Shapiro S. L., 1981, *Astrophys. J.*, 243, 32  
 Faucher-Giguère C.-A., Kereš D., Ma C.-P., 2011, *Mon. Not. R. Astron. Soc.*, 417, 2982

- Faucher-Giguere C.-a., Hopkins P. F., Kere D., Muratov A. L., Quataert E., Murray N., 2015, *Mon. Not. R. Astron. Soc.*, 449, 987
- Faucher-Giguere C.-A., Feldmann R., Quataert E., Kereš D., Hopkins P. F., Murray N., 2016, *Mon. Not. R. Astron. Soc. Lett.*, 461, L32
- Feldmann R., 2013, *Mon. Not. R. Astron. Soc.*, 433, 1910
- Feldmann R., Mayer L., 2015, *Mon. Not. R. Astron. Soc.*, 446, 1939
- Feldmann R., Carollo C. M., Mayer L., Renzini A., Lake G., Quinn T., Stinson G. S., Yepes G., 2010, *Astrophys. J.*, 709, 218
- Feldmann R., Carollo C. M., Mayer L., 2011, *Astrophys. J.*, 736, 88
- Feldmann R., Hopkins P. F., Quataert E., Faucher-Giguere C.-A., Kereš D., 2016, *Mon. Not. R. Astron. Soc. Lett.*, 458, L14
- Förster Schreiber N. M., et al., 2009, *Astrophys. J.*, 706, 1364
- Freeman J. B., Dale R., 2013, *Behav. Res. Methods*, 45, 83
- Furlong M., et al., 2015, *Mon. Not. R. Astron. Soc.*, 450, 4486
- Gabor J. M., Davé R., 2012, *Mon. Not. R. Astron. Soc.*, 427, 1816
- Garrison-Kimmel S., Bullock J. S., Boylan-Kolchin M., Bardwell E., 2016, 13, 1
- Genzel R., et al., 2015, *Astrophys. J.*, 800, 20
- Gill S. P. D., Knebe A., Gibson B. K., 2004, *Mon. Not. R. Astron. Soc.*, 351, 399
- Gobat R., et al., 2017
- Guedes J., Callegari S., Madau P., Mayer L., 2011, *Astrophys. J.*, 742, 76
- Gunn J. E., Gott J. R., 1972, *Astrophys. J.*, 176, 1
- Hafen Z., et al., 2016, 000
- Hahn O., Abel T., 2011, *Mon. Not. R. Astron. Soc.*, 415, 2101
- Hahn O., Porciani C., Dekel A., Carollo C. M., 2009, *Mon. Not. R. Astron. Soc.*, 398, 1742
- Hahn O., Martizzi D., Wu H.-Y., Evrard A. E., Teyssier R., Wechsler R. H., 2015, preprint, 000, 21 ([arXiv:1509.04289](https://arxiv.org/abs/1509.04289))
- Hartigan J. A., Hartigan P. M., 1985, *Ann. Stat.*, 13, 70
- Hearin A. P., Watson D. F., 2013, *Mon. Not. R. Astron. Soc.*, 435, 1313
- Hearin A. P., Behroozi P. S., van den Bosch F. C., 2016, *Mon. Not. R. Astron. Soc.*, 461, 2135
- Hinshaw G., et al., 2013, *Astrophys. J. Suppl. Ser.*, 208, 19
- Hopkins P. F., 2013, *Mon. Not. R. Astron. Soc.*, 428, 2840
- Hopkins P. F., 2015, *Mon. Not. R. Astron. Soc.*, 450, 53
- Hopkins P. F., Hernquist L., Cox T. J., Di Matteo T., Robertson B., Springel V., 2006, *Astrophys. J. Suppl. Ser.*, 163, 1
- Hopkins P. F., Cox T. J., Kereš D., Hernquist L., 2008, *Astrophys. J. Suppl. Ser.*, 175, 390
- Hopkins P. F., Quataert E., Murray N., 2011, *Mon. Not. R. Astron. Soc.*, 417, 950
- Hopkins P. F., Narayanan D., Murray N., 2013, *Mon. Not. R. Astron. Soc.*, 432, 2647
- Hopkins P. F., Kere D., Onorbe J., Faucher-Giguere C.-A., Quataert E., Murray N., Bullock J. S., 2014, *Mon. Not. R. Astron. Soc.*, 445, 581
- Johnston R., Vaccari M., Jarvis M., Smith M., Giovannoli E., Häußler B., Prescott M., 2015, *Mon. Not. R. Astron. Soc.*, 453, 2540
- Jones T. A., Swinbank A. M., Ellis R. S., Richard J., Stark D. P., 2010, *Mon. Not. R. Astron. Soc.*, 404, 1247
- Kashino D., et al., 2013, *Astrophys. J.*, 777, L8
- Kauffmann G., et al., 2003, *Mon. Not. R. Astron. Soc.*, 341, 54
- Kawata D., Mulchaey J. S., 2008, *Astrophys. J.*, 672, L103
- Keres D., Katz N., Weinberg D. H., Dave R., 2005, *Mon. Not. R. Astron. Soc.*, 363, 2
- Knollmann S. R., Knebe A., 2009, *Astrophys. J. Suppl. Ser.*, 182, 608
- Kormendy J., Ho L. C., 2013, *Annu. Rev. Astron. Astrophys.*, 51, 511
- Kovac K., et al., 2014, *Mon. Not. R. Astron. Soc.*, 438, 717
- Kravtsov A., Vikhlinin A., Meshcheryakov A., 2014
- Kriek M., et al., 2006, *Astrophys. J.*, 649, L71
- Krumholz M. R., Gnedin N. Y., 2011, *Astrophys. J.*, 729, 36
- Labbe I., et al., 2005, *Astrophys. J.*, 624, L81
- Larson R. B., Tinsley B. M., Caldwell C. N., 1980, *Astrophys. J.*, 237, 692
- Leauthaud A., et al., 2012, *Astrophys. J.*, 744, 159
- Leitherer C., et al., 1999, *Astrophys. J. Suppl. Ser.*, 123, 3
- Lilly S. J., Carollo C. M., Pipino A., Renzini A., Peng Y., 2013, *Astrophys. J.*, 772, 119
- Ma X., Hopkins P. F., Faucher-Giguere C.-A., Zolman N., Muratov A. L., Kereš D., Quataert E., 2016, *Mon. Not. R. Astron. Soc.*, 456, 2140
- Magdis G. E., Rigopoulou D., Huang J.-S., Fazio G. G., 2010, *Mon. Not. R. Astron. Soc.*, 401, 1521
- Man A. W. S., et al., 2016, *Astrophys. J.*, 820, 11
- Mancini C., Renzini A., Daddi E., Rodighiero G., Berta S., Grogin N., Kocevski D., Koekemoer A., 2015, *Mon. Not. R. Astron. Soc.*, 450, 763
- Marchesini D., et al., 2014, *Astrophys. J.*, 794, 65
- Martins N. S., et al., 2016, *Astrophys. J.*, 827, L25
- Martizzi D., Teyssier R., Moore B., 2012, *Mon. Not. R. Astron. Soc.*, 420, 2859
- McBride J., Fakhouri O., Ma C.-P., 2009, *Mon. Not. R. Astron. Soc.*, 398, 1858
- McCarthy I. G., Frenk C. S., Font A. S., Lacey C. G., Bower R. G., Mitchell N. L., Balogh M. L., Theuns T., 2008, *Mon. Not. R. Astron. Soc.*, 383, 593
- McCracken H. J., et al., 2012, *Astron. Astrophys.*, 544, A156
- McGee S. L., Balogh M. L., Wilman D. J., Bower R. G., Mulchaey J. S., Parker L. C., Oemler A., 2011, *Mon. Not. R. Astron. Soc.*, 413, 996
- Moore B., Katz N., Lake G., Dressler A., Oemler A., 1996, *Nature*, 379, 613
- More S., van den Bosch F. C., Cacciato M., Mo H. J., Yang X., Li R., 2009, *Mon. Not. R. Astron. Soc.*, 392, 801
- More S., van den Bosch F. C., Cacciato M., Skibba R., Mo H. J., Yang X., 2011, *Mon. Not. R. Astron. Soc.*, 410, 210
- Moster B. P., Naab T., White S. D. M., 2013, *Mon. Not. R. Astron. Soc.*, 428, 3121
- Munshi F., et al., 2013, *Astrophys. J.*, 766, 56
- Muratov A. L., Kereš D., Faucher-Giguere C.-A., Hopkins P. F., Quataert E., Murray N., 2015, *Mon. Not. R. Astron. Soc.*, 454, 2691
- Muzzin A., et al., 2013a, *Astrophys. J. Suppl. Ser.*, 206, 8
- Muzzin A., et al., 2013b, *Astrophys. J.*, 777, 18
- Naab T., Johansson P. H., Ostriker J. P., Efstathiou G., 2007, *Astrophys. J.*, 658, 710
- Naab T., Johansson P. H., Ostriker J. P., 2009, *Astrophys. J.*, 699, L178
- Narayanan D., et al., 2015, *Nature*, 525, 496
- Noeske K. G., et al., 2007, *Astrophys. J.*, 660, L43
- Oklopčić A., Hopkins P. F., Feldmann R., Keres D., Faucher-Giguere C.-A., Murray N., 2016, 16, 1
- Oñorbe J., Boylan-Kolchin M., Bullock J. S., Hopkins P. F., Kereš D., Faucher-Giguere C.-A., Quataert E., Murray N., 2015, *Mon. Not. R. Astron. Soc.*, 454, 2092
- Oser L., Ostriker J. P., Naab T., Johansson P. H., Burkert A., 2010, *Astrophys. J.*, 725, 2312
- Pannella M., et al., 2015, *Astrophys. J.*, 807, 141
- Park C., Choi Y.-Y., Vogeley M. S., Gott III J. R., Blanton M. R., 2007, *Astrophys. J.*, 658, 898
- Pei Y. C., 1992, *Astrophys. J.*, 395, 130
- Peng Y.-j., et al., 2010, *Astrophys. J.*, 721, 193
- Price D. J., 2008, *J. Comput. Phys.*, 227, 10040
- Price S. H., et al., 2014, *Astrophys. J.*, 788, 86
- Ragone-Figueroa C., Granato G. L., Murante G., Borgani S., Cui W., 2013, *Mon. Not. R. Astron. Soc.*, 436, 1750
- Reddick R. M., Wechsler R. H., Tinker J. L., Behroozi P. S., 2013, *Astrophys. J.*, 771, 30
- Reddy N. a., Pettini M., Steidel C. C., Shapley A. E., Erb D. K., Law D. R., 2012, *Astrophys. J.*, 754, 25
- Rodighiero G., et al., 2010, *Astron. Astrophys.*, 518, L25
- Rodríguez-Puebla A., Primack J. R., Behroozi P., Faber S. M., 2016, *Mon. Not. R. Astron. Soc.*, 455, 2592
- Saintonge A., et al., 2011, *Mon. Not. R. Astron. Soc.*, 415, 61
- Saintonge A., et al., 2013, *Astrophys. J.*, 778, 2
- Salmon B., et al., 2015, *Astrophys. J.*, 799, 183
- Sánchez Almeida J., Elmegreen B. G., Muñoz-Tuñón C., Elmegreen D. M., 2014, *Astron. Astrophys. Rev.*, 22, 71
- Santini P., et al., 2012, *Astron. Astrophys.*, 538, A33
- Sargent M., et al., 2015, *Astrophys. J.*, 806, L20
- Scannapieco C., et al., 2012, *Mon. Not. R. Astron. Soc.*, 423, 1726



Schaye J., et al., 2010, *Mon. Not. R. Astron. Soc.*, 402, 1536  
Schaye J., et al., 2015, *Mon. Not. R. Astron. Soc.*, 446, 521  
Schiminovich D., et al., 2010, *Mon. Not. R. Astron. Soc.*, 408, 919  
Schinnerer E., et al., 2016, *Astrophys. J.*, 833, 112  
Schreiber C., et al., 2015, *Astron. Astrophys.*, 575, A74  
Scoville N., et al., 2016, *Astrophys. J.*, 820, 83  
Seko A., Ohta K., Yabe K., Hatsukade B., Akiyama M., Iwamuro F., Tamura N., Dalton G., 2016, *Astrophys. J.*, 819, 82  
Serra P., et al., 2012, *Mon. Not. R. Astron. Soc.*, 422, 1835  
Shankar F., et al., 2014, *Astrophys. J.*, 797, L27  
Shivaei I., et al., 2015, *Astrophys. J.*, 815, 98  
Somerville R. S., Davé R., 2015, *Annu. Rev. Astron. Astrophys.*, 53, 150421145606007  
Sparre M., et al., 2015, *Mon. Not. R. Astron. Soc.*, 447, 3548  
Sparre M., Hayward C. C., Feldmann R., Faucher-Giguère C.-A., Muratov A. L., Kereš D., Hopkins P. F., 2016, arXiv  
Speagle J. S., Steinhardt C. L., Capak P. L., Silverman J. D., 2014, *Astrophys. J. Suppl. Ser.*, 214, 15  
Springel V., Di Matteo T., Hernquist L., 2005, *Astrophys. J.*, 620, L79  
Steidel C. C., Adelberger K. L., Giavalisco M., Dickinson M., Pettini M., 1999, *Astrophys. J.*, 519, 1  
Straatman C. M. S., et al., 2014, *Astrophys. J.*, 783, L14  
Strateva I., et al., 2001, *Astron. J.*, 122, 1861  
Tacchella S., Dekel A., Carollo C. M., Ceverino D., DeGraf C., Lapiner S., Mandelker N., Primack Joel R., 2016, *Mon. Not. R. Astron. Soc.*, 457, 2790  
Tacconi L. J., et al., 2013, *Astrophys. J.*, 768, 74  
Tasitsiomi A., Kravtsov A. V., Gottlober S., Klypin A. A., 2004, *Astrophys. J.*, 607, 125  
Thomas D., Maraston C., Schawinski K., Sarzi M., Silk J., 2010, *Mon. Not. R. Astron. Soc.*, 1789, 1775  
Tomczak A. R., et al., 2014, *Astrophys. J.*, 783, 85  
Tomczak A. R., et al., 2016, *Astrophys. J.*, 817, 118  
Trayford J. W., Theuns T., Bower R. G., Crain R. A., Lagos C. d. P., Schaller M., Schaye J., 2016, *Mon. Not. R. Astron. Soc.*, p. stw1230  
Trujillo I., et al., 2006, *Astrophys. J.*, 650, 18  
Valentinuzzi T., et al., 2010, *Astrophys. J.*, 721, L19  
Van Den Bosch F. C., Aquino D., Yang X., Mo H. J., Pasquali A., McIntosh D. H., Weinmann S. M., Kang X., 2008, *Mon. Not. R. Astron. Soc.*, 387, 79  
Vogelsberger M., et al., 2014, *Mon. Not. R. Astron. Soc.*, 444, 1518  
Wang H. Y., Mo H. J., Jing Y. P., 2007, *Mon. Not. R. Astron. Soc.*, 375, 633  
Wang L., Dutton A. A., Stinson G. S., Macciò A. V., Penzo C., Kang X., Keller B. W., Wadsley J., 2015, *Mon. Not. R. Astron. Soc.*, 454, 83  
Weinmann S. M., Kauffmann G., von der Linden A., De Lucia G., 2010, *Mon. Not. R. Astron. Soc.*, 406, 2249  
Weinmann S. M., Neistein E., Dekel A., 2011, *Mon. Not. R. Astron. Soc.*, 417, 2737  
Wellons S., et al., 2016, *Mon. Not. R. Astron. Soc.*, 456, 1030  
Whitaker K. E., et al., 2011, *Astrophys. J.*, 735, 86  
Whitaker K. E., van Dokkum P. G., Brammer G., Franx M., 2012, *Astrophys. J.*, 754, L29  
Wiersma R. P. C., Schaye J., Smith B. D., 2009, *Mon. Not. R. Astron. Soc.*, 393, 99  
Wijesinghe D. B., et al., 2012, *Mon. Not. R. Astron. Soc.*, 423, 3679  
Wild V., Charlot S., Brinchmann J., Heckman T., Vince O., Pacifici C., Chevallard J., 2011, *Mon. Not. R. Astron. Soc.*, 417, 1760  
Williams R. J., Quadri R. F., Franx M., van Dokkum P., Labbé I., 2009, *Astrophys. J.*, 691, 1879  
Williams R. J., Quadri R. F., Franx M., van Dokkum P., Toft S., Kriek M., Labbé I., 2010, *Astrophys. J.*, 713, 738  
Wisnioski E., et al., 2014, *Astrophys. J.*, 799, 209  
Wuyts S., et al., 2007, *Astrophys. J.*, 655, 51  
Yang X., Mo H. J., van den Bosch F. C., 2009, *Astrophys. J.*, 695, 900  
Yang X., Mo H. J., van den Bosch F. C., Zhang Y., Han J., 2012, *Astrophys. J.*, 752, 41  
Yang X., Mo H. J., van den Bosch F. C., Bonaca A., Li S., Lu Y., Lu Y., Lu Z., 2013, *Astrophys. J.*, 770, 115

Yoshikawa T., et al., 2010, *Astrophys. J.*, 718, 112  
van Dokkum P. G., et al., 2015, *Astrophys. J.*, 813, 23  
van Uitert E., et al., 2016, *Mon. Not. R. Astron. Soc.*, 459, 3251  
van de Voort F., Schaye J., Booth C. M., Haas M. R., Dalla Vecchia C., 2011, *Mon. Not. R. Astron. Soc.*, 414, 2458  
van de Voort F., Quataert E., Hopkins P. F., Faucher-Giguère C.-A., Feldmann R., Kereš D., Chan T. K., Hafen Z. H., 2016, *Mon. Not. R. Astron. Soc.*, 12, stw2322  
van der Wel A., et al., 2014a, *Astrophys. J.*, 788, 28  
van der Wel A., et al., 2014b, *Astrophys. J.*, 792, L6

## APPENDIX A: COLOUR BIMODALITY

### A1 Comparison with UltraVISTA

We make use of the UltraVISTA survey (McCracken et al. 2012) to support our statement that the colours of the simulated galaxies are in reasonable (but far from perfect) agreement with observations. Specifically, we use version 4.1 of the K-band selected catalog<sup>6</sup> (Muzzin et al. 2013a). The full catalog contains 262615 sources. We discard stars and objects that are near bright sources ( $USE = 1$ ,  $nan\_contam = 0$ ,  $K\_flag \leq 2$ ), and only use sources with a total K band magnitude brighter than 23.4 corresponding to the 90% flux completeness limit. To approximately match the properties of the MASSIVEFIRE sample we only select UltraVISTA galaxies with  $1.6 < z < 2.1$  and with stellar masses in the range  $10^{10} - 10^{11} M_{\odot}$ . This selection results in 7493 galaxies. While UltraVISTA is, e.g., 0.6 mag deeper than NMBS (Whitaker et al. 2011), it is not quite mass-complete down to  $M_{star} \sim 10^{10} M_{\odot}$  at  $z \sim 2$ . In fact, the 95% mass completeness limit is  $1.3 \times 10^{10} M_{\odot}$  at  $z = 1.6$  and  $3.1 \times 10^{10} M_{\odot}$  at  $z = 2.1$ . However, as we show below the large sample size of UltraVISTA helps in detecting a bimodal signal with high statistical significance.

For the bimodality test we further restrict galaxies to fall within a range of rest-frame  $U - V$  and  $V - J$  colours, effectively excluding the dustiest galaxies with extremely red V-J colours that are absent in the MASSIVEFIRE sample. This final selection ( $0.2 < V - J < 1.2$ ,  $0.5 < U - V < 2$ ) brings the number of UltraVISTA galaxies down to 4821.

We compare the UltraVISTA and MASSIVEFIRE samples in Fig. A1. While the colours of the simulated galaxies generally overlap with the colours of observed galaxies, they are distributed differently. In particular, our simulations lack galaxies with U-V rest-frame colours above 1.6. Also, the colours of the star forming galaxies are somewhat closer ( $\sim 0.2$  mag) to the star forming vs. quiescent separation line in our simulations than in observations.

We note, however, that this “bye-eye” comparison is simplistic and suffers from important systematics. First, there are systematic uncertainties of  $\sim 0.1$  mag regarding the zero-points in the various observational filters (Muzzin et al. 2013a). In addition, rest-frame fluxes are derived from integrating the best-fit spectral energy distribution. Hence, systematic effects enter via photo-metric redshift estimates and template selections. Second, our approach of accounting for dust absorption is relatively simplistic and likely introduces a non-significant systematic error. Third, we note that the U-V and V-J colours of our simulated galaxies are not precisely matched to the UltraVISTA observations. There are differences in

<sup>6</sup> <http://www.strw.leidenuniv.nl/galaxyevolution/ULTRAVISTA/Ultravista/K-selected.html>

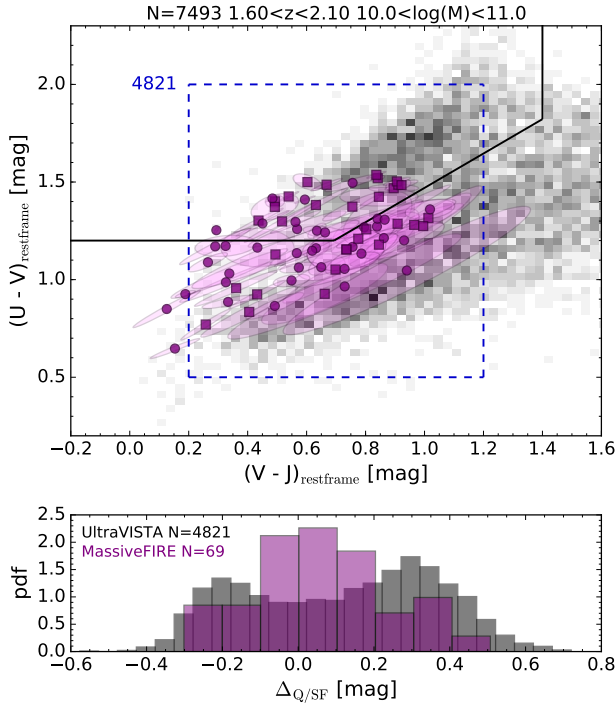


**Figure A1.** Distribution of galaxy colours in UltraVISTA and in MASSIVEFIRE. (Top) Restframe U–V and V–J diagram. The shaded background shows the distribution of  $1.6 < z < 2.1$  galaxies selected from the UltraVISTA catalog (see text) on a linear grey scale. Squares and circles denote the average rest-frame colours of MASSIVEFIRE galaxies at  $z = 1.7$  and  $z = 2$  respectively. Semi-transparent ellipses show the  $1 - \sigma$  variations of the mean colours with changing lines-of-sight. The solid line is the dividing line between quiescent (to the top and left) and star forming (to the bottom and right) galaxies (Whitaker et al. 2011). (Bottom) Normalized distribution of  $\Delta_{Q/SF}$ , the distance of a source in U–V, V–J space to the quiescent vs. star forming dividing line. We use the 4821 UltraVISTA galaxies with colours that place them inside the region enclosed by the dashed line in the top panel. For MASSIVEFIRE we compute the median value of  $\Delta_{Q/SF}$  (over 50 random lines of sight) for each galaxy and we combine the  $z = 1.7$  and  $z = 2$  snapshots resulting in 69 sources. While the colours of the simulated galaxies generally overlap with the colours of observed galaxies, their statistical distributions appear to be different, see text for a more detailed discussion. In addition, UltraVISTA galaxies show a clear bimodal signal in  $\Delta_{Q/SF}$ , while no such signal is apparent in our simulations. However, the lack of a strong bimodal signal is expected given the modest size of our sample, see text.

the aperture size<sup>7</sup>, in the adopted extinction law, and in the precise shape of the U, V, and J filter transmission curves. Fourth, our sample was selected to cover a broad range of halo growth histories (§2.3) and is thus not necessarily representative of a purely mass-selected sample. Clearly, additional work is required to fully determine the importance of the apparent differences in the colour distributions.

The presence or absence of a colour-bimodality should be somewhat less dependent on systematic colour shifts. The bottom panel in Fig. A1 compares the distributions of  $\Delta_{Q/SF}$ , the distance

of a source in U–V, V–J space to the quiescent vs. star forming dividing line, in our simulations with those in UltraVISTA. The latter show a clear bimodality, while no such bimodality is apparent in our sample of simulated galaxies. We note, however, that the UltraVISTA sample (after selecting galaxies with masses and redshifts similar to our simulated sample) is 2 orders of magnitude larger. Hence, a reasonable question is whether we should expect to see a bimodality signal given the modest size of the MASSIVEFIRE sample.

## A2 Testing for multi-modality in the colour distributions

We apply the dip test (Hartigan & Hartigan 1985) to the distribution of  $\Delta_{Q/SF}$  and to the distribution of the U–V rest-frame colour in UltraVISTA. Specifically, we use the subset of 4821 UltraVISTA galaxies with redshifts, stellar masses, and colours in broad agreement with those of our simulated set of galaxies. The dip test allows us to decide whether the distributions are significantly different from unimodal distributions. The dip test compares favourably with other approaches aimed at quantifying multi-modality, see, e.g., Freeman & Dale (2013). It is available as a package<sup>8</sup> for the R Project for Statistical Computing<sup>9</sup>.

We first choose a sample size (ranging from 8 to 4821 objects) and then generate 1000 samples of this size drawn randomly with replacement from the selected UltraVISTA subset. We run the dip test on each of the 1000 samples and record how many samples show evidence of multi-modality, i.e., the number of samples that have a  $p$  value below  $\alpha = 0.05$ .

Fig. A2 shows how the sample size affects the likelihood of detecting a multi-modality in the  $\Delta_{Q/SF}$  and U–V distributions. Samples containing several hundreds (several thousands) of galaxies offer a 50% chance of confirming a multi-modal  $\Delta_{Q/SF}$  (U–V) distribution at the  $\alpha = 0.05$  significance level. The size of the MASSIVEFIRE sample ( $\sim 70$  galaxies if we combine the  $z = 1.7$  and  $z = 2$  redshifts) is too small to reliably detect a bimodality, even if our simulated galaxies had colour distributions that mirrored those of UltraVISTA.

According to Fig. A2, it is significantly easier to detect bimodality in the  $\Delta_{Q/SF}$  distribution than in the U–V rest-frame colour distribution. Clearly, a careful choice of the observable can significantly boost the likelihood of detecting a bimodality in the underlying data set.

## APPENDIX B: ADDITIONAL TABLES

Table B1 is similar to Table 2 but shows the properties of our simulated galaxies at  $z = 1.7$ . Table B2 provides results from a linear regression analysis of the stellar mass – halo mass relation, supplementing the discussion in §3.6.

<sup>7</sup> Colours in UltraVISTA are measured within a 2.1 arcsecond diameter aperture (aperture radius of  $\sim 9$  kpc for galaxies in the considered redshift range), while we measure colours within a circular aperture of 5 kpc radius.

<sup>8</sup> <https://cran.r-project.org/web/packages/diptest/index.html>

<sup>9</sup> <https://www.r-project.org>

Name	Central/Satellite	$\log_{10} M_{180\text{m}}$ ( $\log_{10} M_{\odot}$ )	$R_{\text{halo}}$ (kpc)	$\log_{10} M_{\text{star}}$ ( $\log_{10} M_{\odot}$ )	SFR ( $M_{\odot} \text{ yr}^{-1}$ )	$\log_{10} \text{sSFR}$ ( $\log_{10} \text{ yr}^{-1}$ )	U-V (mag)	V-J (mag)	$f_{\text{Q}}$ (%)
A1:0	Central	12.44	171.1	10.47	11.5	-9.31	1.467	0.913	84
A2:0	Central	12.62	197.1	10.66	19.2	-9.19	1.314	1.018	0
A3:0	Central	12.45	173.0	10.31	0.5	-10.45	1.297	0.422	100
A4:0	Central	12.52	182.4	10.46	6.0	-9.43	1.259	0.785	38
A5:0	Central	12.45	172.2	10.34	0.0	-11.84	1.422	0.534	100
A6:0	Central	12.58	190.9	10.47	8.6	-9.38	1.478	0.917	100
A7:0	Central	12.85	235.3	10.55	16.2	-8.97	1.315	0.994	0
A8:0	Central	12.82	229.9	10.48	13.2	-8.84	0.895	0.650	0
A9:0	Central	12.87	238.7	10.07	1.6	-9.69	1.373	0.613	100
A9:1	Satellite	11.99	75.7	10.40	42.3	-8.67	0.732	0.223	0
A10:0	Central	12.77	220.9	10.64	30.3	-8.79	0.928	0.318	0
B1:0	Central	12.96	255.7	11.00	27.0	-9.32	1.285	0.897	8
B2:0	Central	13.09	283.1	10.92	3.9	-10.10	1.519	0.844	100
B3:0	Central	13.16	297.1	10.91	51.5	-8.88	0.891	0.387	0
B3:1	Satellite	10.79	21.9	9.62	0.0	-11.92	1.409	0.484	100
B4:0	Central	12.92	248.3	10.68	22.8	-8.95	1.294	1.022	0
B4:1	Central	12.20	142.4	10.14	12.3	-8.52	0.844	0.390	0
B4:2	Central	12.02	124.5	10.19	0.5	-10.32	1.304	0.512	86
B4:3	Satellite	11.90	51.0	10.06	0.3	-10.62	1.477	0.649	100
B5:0	Central	13.01	265.0	10.84	17.5	-9.29	1.171	0.843	0
B5:1	Satellite	11.12	21.8	9.64	0.0	-12.56	1.512	0.590	98
Cm3:0	Central	13.78	478.6	11.68	112.7	-9.37	1.164	0.698	12
Cm3:1	Satellite	12.48	67.2	11.28	35.4	-9.68	1.428	0.817	84
Cm3:3	Satellite	11.96	94.9	10.67	57.7	-8.84	1.213	0.768	4
Cm3:4	Satellite	11.53	35.7	10.61	15.5	-9.45	1.505	0.905	100
Cm3:5	Satellite	11.84	62.5	10.21	11.9	-9.10	1.054	0.654	0
Cm3:6	Satellite	11.50	51.8	10.06	5.1	-9.34	1.027	0.336	22
Cm3:7	Central	11.64	92.8	10.07	2.7	-9.46	1.380	0.764	100
Cm3:8	Satellite	11.32	72.2	10.32	1.9	-10.04	1.536	0.837	100
Cm3:9	Satellite	11.56	87.3	10.50	8.0	-9.52	1.484	0.924	100
Cm3:10	Satellite	10.78	27.4	10.00	0.0	-12.54	1.404	0.485	98

**Table B1.** Properties of MASSIVEFIRE galaxies at  $z = 1.7$ . Columns refer to the same quantities as in Table 2.

redshift	$\log_{10} M_{180\text{m}}$ ( $\log_{10} M_{\odot}$ )	$\langle \log_{10} M_{180\text{m}} \rangle$ ( $\log_{10} M_{\odot}$ )	$\langle \log_{10} M_{\text{star}} \rangle$ ( $\log_{10} M_{\odot}$ )	slope	scatter (dex)	remark
9.2	9.0 – 11.0	9.90	6.76	$1.96^{+0.18}_{-0.15}$	$0.42^{+0.06}_{-0.04}$	
7.1	9.5 – 11.5	10.50	7.87	$1.58^{+0.13}_{-0.11}$	$0.26^{+0.04}_{-0.01}$	
5.1	10.0 – 12.0	11.15	8.66	$1.26^{+0.11}_{-0.10}$	$0.26^{+0.03}_{-0.02}$	
3.0	10.5 – 13.0	12.06	9.89	$0.89^{+0.15}_{-0.13}$	$0.25^{+0.04}_{-0.02}$	
2.0	11.5 – 14.0	12.59	10.51	$0.91^{+0.13}_{-0.10}$	$0.23^{+0.05}_{-0.02}$	
2.0	11.5 – 14.0	12.47	10.32	$0.93^{+0.13}_{-0.10}$	$0.15^{+0.12}_{-0.02}$	quiescent
2.0	11.5 – 14.0	12.63	10.57	$0.89^{+0.13}_{-0.10}$	$0.24^{+0.05}_{-0.02}$	star forming
1.7	12.0 – 14.0	12.80	10.66	$0.88^{+0.08}_{-0.08}$	$0.19^{+0.08}_{-0.04}$	
1.7	12.0 – 14.0	12.56	10.39	$0.42^{+0.52}_{-0.31}$	$0.21^{+0.15}_{-0.02}$	quiescent
1.7	12.0 – 14.0	12.95	10.81	$0.97^{+0.07}_{-0.04}$	$0.12^{+0.03}_{-0.01}$	star forming
2.0	12.3 – 12.6	12.45	10.28	–	$0.17^{+0.04}_{-0.02}$	
2.0	12.3 – 12.6	12.45	10.26	–	$0.16^{+0.11}_{-0.02}$	quiescent
2.0	12.3 – 12.6	12.45	10.29	–	$0.18^{+0.05}_{-0.02}$	star forming
2.0	12.8 – 13.2	12.97	10.86	–	$0.21^{+0.09}_{-0.04}$	

**Table B2.** Properties of the SHMR of central galaxies for various redshifts and halo mass ranges (first two columns). Columns 3 and 4 show the average of the logarithms of the halo and stellar masses, respectively. The fifth column shows the slope of the linear regression:  $\log_{10} M_{\text{star}} = \text{slope} (\log_{10} M_{180\text{m}} - \langle \log_{10} M_{180\text{m}} \rangle) + \langle \log_{10} M_{\text{star}} \rangle$ . No regression is performed for the last four rows. The penultimate column denotes the scatter of the logarithm of the stellar mass for the given halo mass range. The scatter in the top ten rows is measured relative to the linear regression line, while the bottom four rows report the sample standard deviation of  $\log_{10} M_{\text{star}}$  in narrow bins of halo masses at  $z = 2$ . The final column denotes whether results are shown for a subset (quiescent, star forming) of the total set of central galaxies. Confidence intervals ( $1-\sigma$ ) are computed via bootstrapping.

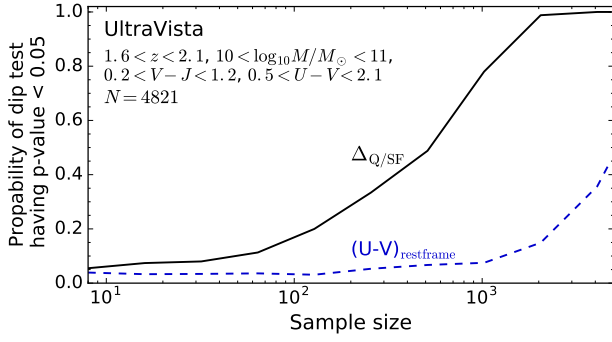


**Figure A2.** Probability of detecting bimodality in the  $\Delta_{Q/SF}$  and  $U-V$  distributions at a significance level of  $\alpha = 0.05$  as function of sample size. It requires many hundreds (for  $\Delta_{Q/SF}$ ) or thousands (for  $U-V$ ) of galaxies drawn randomly from the UltraVISTA parent distribution to find a deviation from uni-modality with high statistical significance (for samples with masses, colours, and redshifts similar to our simulated sample).